Automated Detection and Tracking of Low Latitude Plasma Bubbles Utilizing Global-Scale Observations of the Limb and Disk (GOLD) 135.6 nm Data

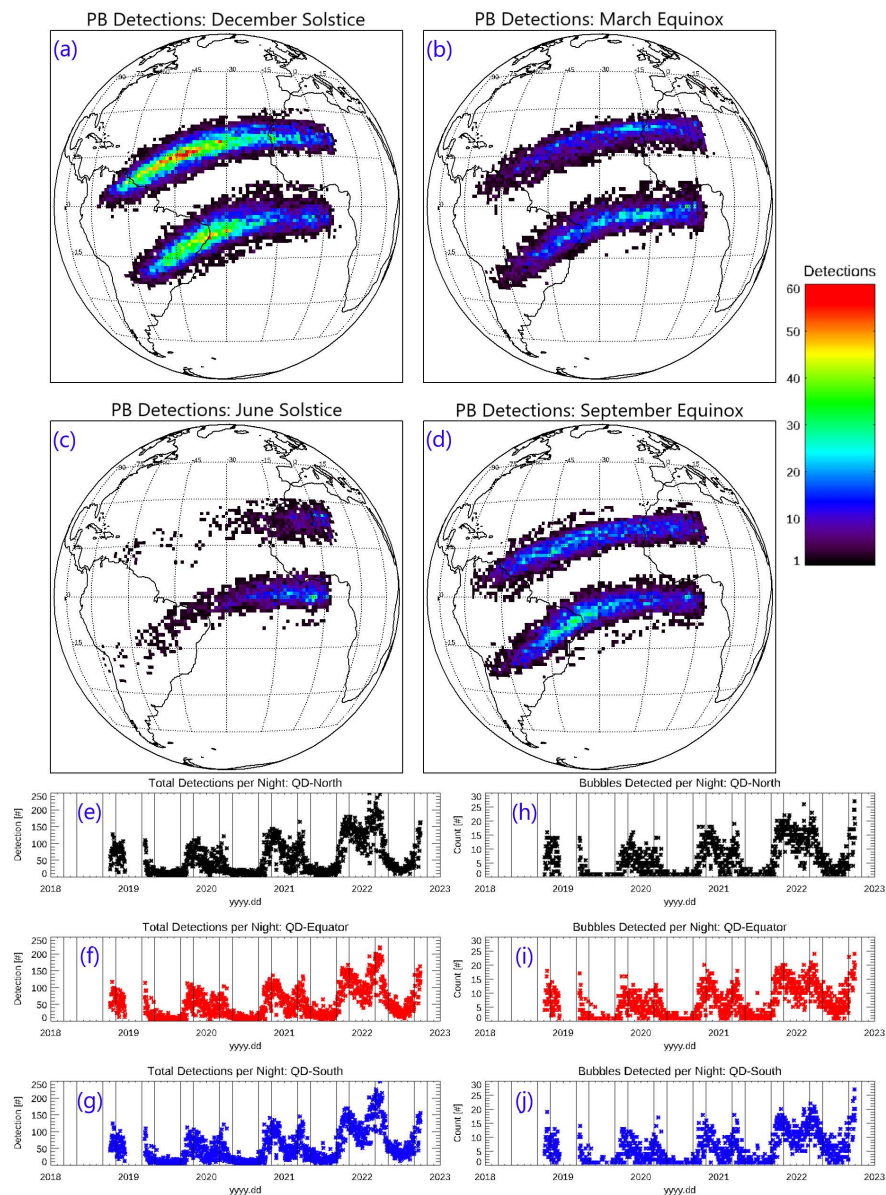Vincent James Adkins[1] and Scott L England[2]

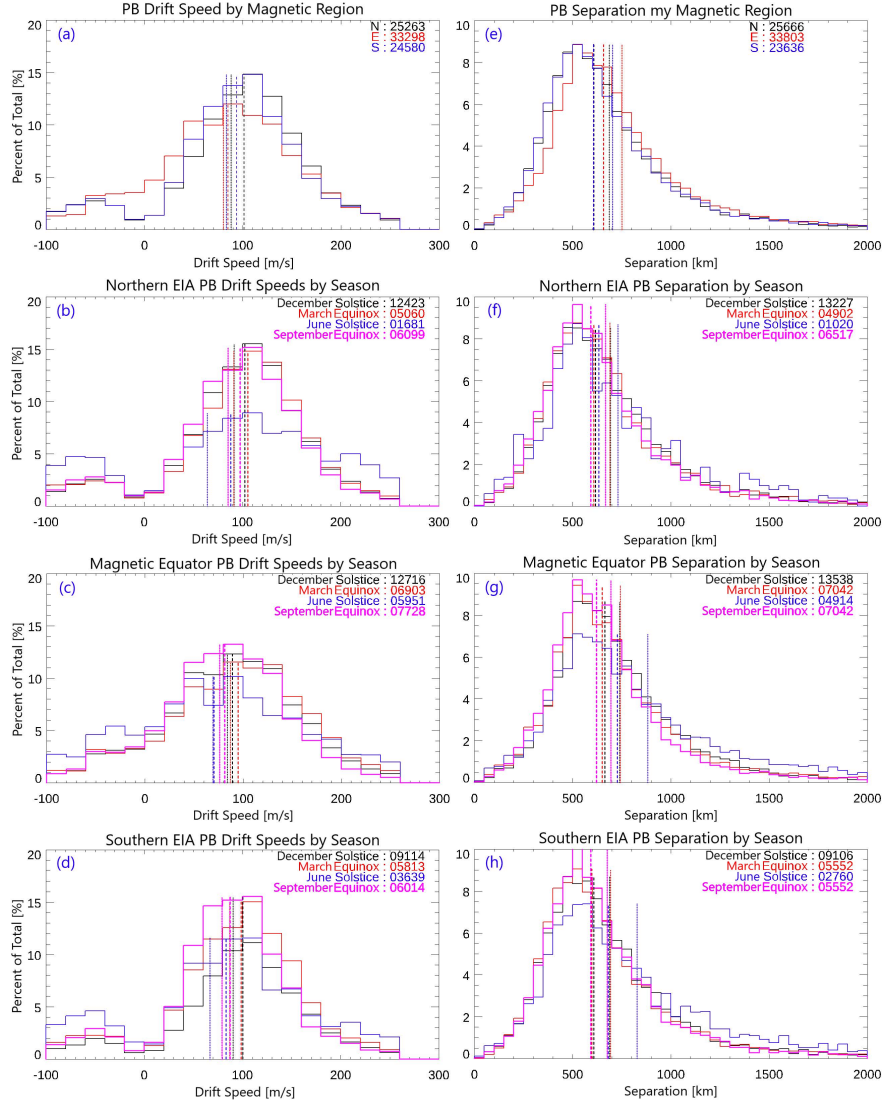[1]Virginia Polytechnic Institute and State Unversity
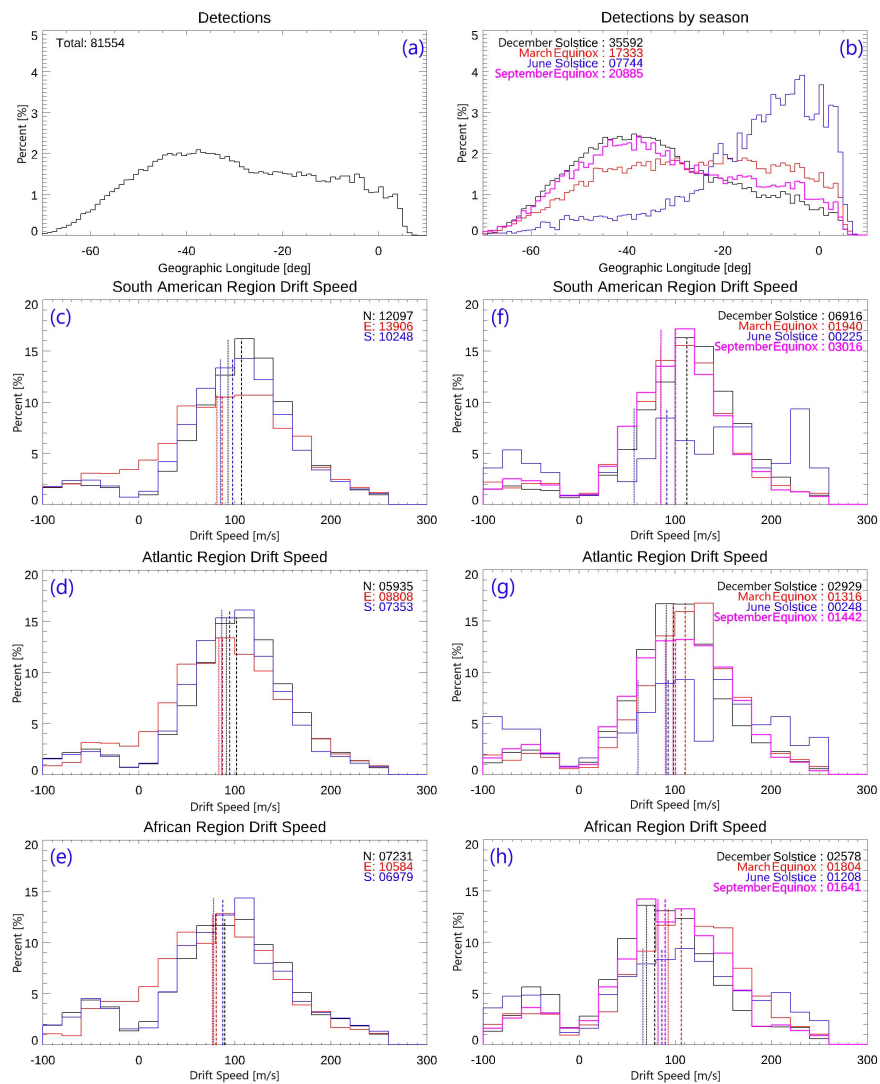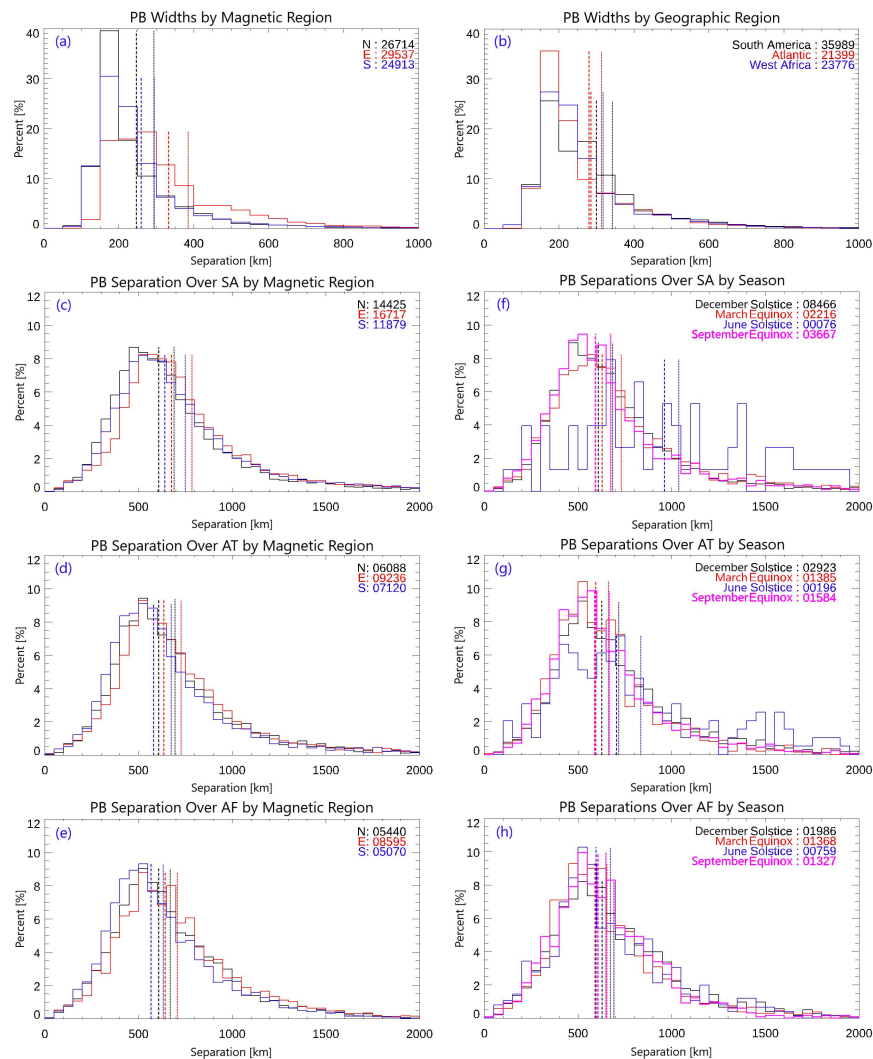[2]Virginia Polytechnic Institute and State University

March 26, 2023

Abstract

Plasma bubbles are regions of depleted plasma within the upper thermosphere/ionosphere that form during post-sunset hours near the magnetic equator. These structures tend to align with local geomagnetic field lines, extend upwards hundreds of kilometers along geomagnetic longitudes, and thousands of kilometers along geomagnetic latitudes. These large scale plasma density gradients can attenuate lower frequency radio waves, while small scale structures along the walls can interfere with centimeter scale wavelengths via Fresnel and Bragg scattering. Large scale statistical analysis of this phenomenon can further understanding of their occurrence and subsequent behavior. The current study utilizes Global-Scale Observations of the Limb and Disk (GOLD) 135.6 nm nightglow data from October 5, 2018 to September 30, 2022. GOLD has a unique perspective from geostationary orbit, allowing a constant and consistent view of nightglow and structures over the Americas and Atlantic. A plasma bubble detection method is developed and used to generate a database of plasma bubble occurrences. Occurrences are used to calculate plasma bubble drift speeds and separations. Clear seasonality in plasma bubble occurrence rate is evident. Overall occurrences peak during December solstice months and minimize during June solstice for longitudes seen by GOLD. Within GOLD's field of view, higher occurrences are seen to the west during December solstice and east during June solstice. Plasma bubble drift speeds and separations show consistent distributions regardless of magnetic region, geographic region, season, or local time. This suggests plasma bubbles behave consistently and regularly once formed, at least on spatial scales seen by GOLD.
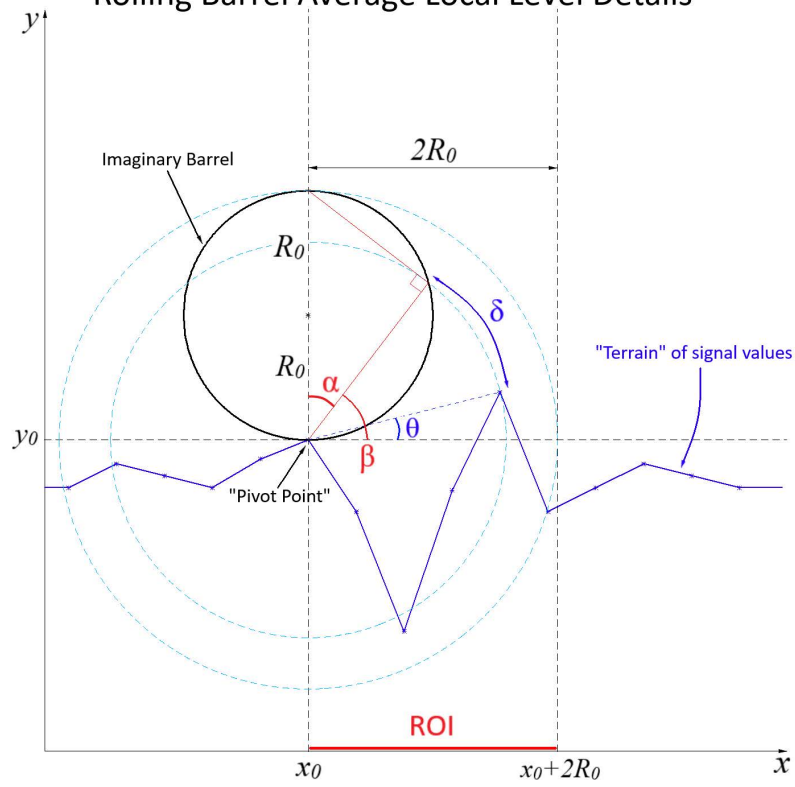
PB Detections: December Solstice

(a)

PB Detections: March Equinox

(b)

PB Detections: June Solstice

(c)

PB Detections: September Equinox

(d)

Detections

Total Detections per Night: QD-North

(e)

Bubbles Detected per Night: QD-North

(h)

Total Detections per Night: QD-Equator

(f)

Bubbles Detected per Night: QD-Equator

(i)

Total Detections per Night: QD-South

(g)

Bubbles Detected per Night: QD-South

(j)

2

Detections

(a)

Total: 81554

Percent [%]

Geographic Longitude [deg]

Detections by season

(b)

December Solstice : 35592
March Equinox : 17333
June Solstice : 07744
September Equinox : 20885

Percent [%]

Geographic Longitude [deg]

South American Region Drift Speed

(c)

N: 12097
E: 13906
S: 10248

Percent [%]

Drift Speed [m/s]

South American Region Drift Speed

(f)

December Solstice : 06916
March Equinox : 01940
June Solstice : 00225
September Equinox : 03016

Percent [%]

Drift Speed [m/s]

Atlantic Region Drift Speed

(d)

N: 05935
E: 08808
S: 07353

Percent [%]

Drift Speed [m/s]

Atlantic Region Drift Speed

(g)

December Solstice : 02929
March Equinox : 01316
June Solstice : 00248
September Equinox : 01442

Percent [%]

Drift Speed [m/s]

African Region Drift Speed

(e)

N: 07231
E: 10584
S: 06979

Percent [%]

Drift Speed [m/s]

African Region Drift Speed

(h)

December Solstice : 02578
March Equinox : 01804
June Solstice : 01208
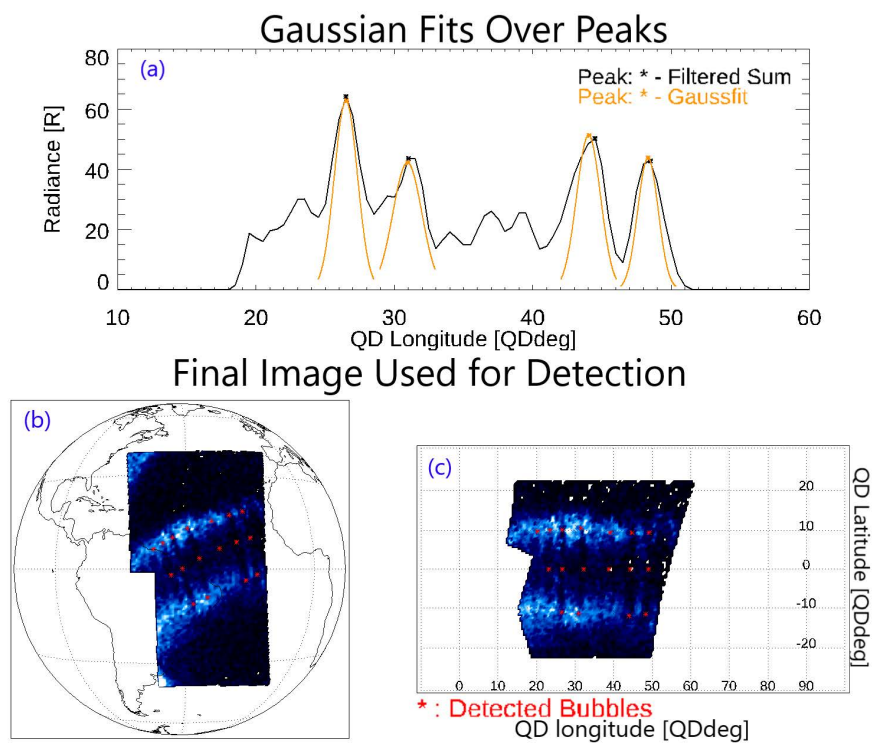September Equinox : 01641

Percent [%]

Drift Speed [m/s]

4

Rolling Barrel Average Local Level Details

Gaussian Fits Over Peaks

(a)

Peak: * - Filtered Sum
Peak: * - Gaussfit

Radiance [R] vs *QD Longitude [QDdeg]*

Final Image Used for Detection

(b)

(c)

QD Latitude [QDdeg]

QD longitude [QDdeg]

*** : Detected Bubbles**

Image Pairs for November 28, 2018

PB Drift Speeds from 2325 to 2340 of November 28, 2018

PB Separations from November 28, 2018 at 2340

Original Data and Interpolants
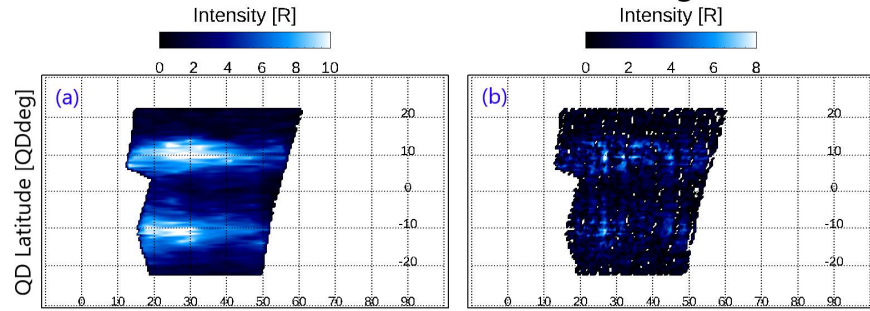

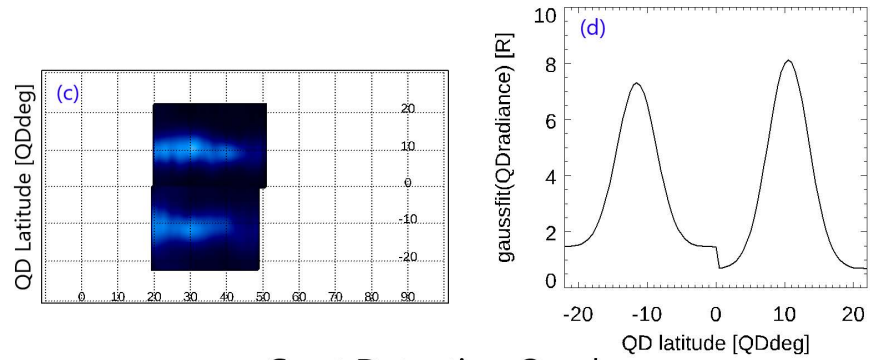## Original Data and Interpolants (Zoomed In)

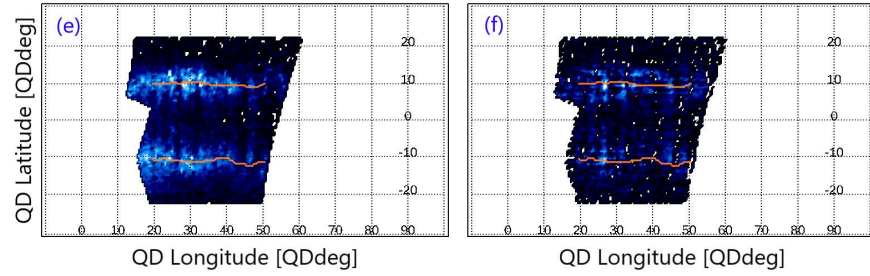## Nearest Neighbor Regions

9

NN Data Pair and QD Conversion

QD and SZA Cutoffs

QD RBAVG and Difference Image

Intensity [R]

Intensity [R]

Crest Detection and Line Plot

Crest Detection Overlays

QD Difference Summation Regions

Southern Sums: Raw and Filtered

Southern Uncertainty Analysis

Smooth Example

(a)

f(x)
Smooth[f(x)] + C
Smooth[f(x)] + C - f(x)

RBAVG Example

(b)

f(x)
RBAVG[f(x)]
RBAVG[f(x)] - f(x)

Radiance Line Plot Along 10 [QDdeg] Latitude

(c)

Radiance
RBAVG
Difference

Automated Detection and Tracking of Low Latitude Plasma Bubbles Utilizing Global-Scale Observations of the Limb and Disk (GOLD) 135.6 nm Data

V. J. Adkins[1], S. L. England[1]

[1]Aerospace and Ocean Engineering, Virginia Polytechnic Institute and State University, Blacksburg, VA, USA

Key Points:

- Plasma bubbles are automatically detected, tracked, and analyzed with a new algorithm
- Four years of GOLD observations are used to generate the largest database of plasma bubble characteristics based on airglow observations
- While plasma bubble occurrence varies with location and season, drift speed, separation, and width are similar

Corresponding author: Vincent Adkins, `vja9999@vt.edu`

Abstract

Plasma bubbles are regions of depleted plasma within the upper thermosphere/ionosphere that form during post-sunset hours near the magnetic equator. These structures tend to align with local geomagnetic field lines, extend upwards hundreds of kilometers along geomagnetic longitudes, and thousands of kilometers along geomagnetic latitudes. These large scale plasma density gradients can attenuate lower frequency radio waves, while small scale structures along the walls can interfere with centimeter scale wavelengths via Fresnel and Bragg scattering. Large scale statistical analysis of this phenomenon can further understanding of their occurrence and subsequent behavior. The current study utilizes Global-Scale Observations of the Limb and Disk (GOLD) 135.6 nm nightglow data from October 5, 2018 to September 30, 2022. GOLD has a unique perspective from geostationary orbit, allowing a constant and consistent view of nightglow and structures over the Americas and Atlantic. A plasma bubble detection method is developed and used to generate a database of plasma bubble occurrences. Occurrences are used to calculate plasma bubble drift speeds and separations. Clear seasonality in plasma bubble occurrence rate is evident. Overall occurrences peak during December solstice months and minimize during June solstice for longitudes seen by GOLD. Within GOLD's field of view, higher occurrences are seen to the west during December solstice and east during June solstice. Plasma bubble drift speeds and separations show consistent distributions regardless of magnetic region, geographic region, season, or local time. This suggests plasma bubbles behave consistently and regularly once formed, at least on spatial scales seen by GOLD.

Plain Language Summary

Plasma bubbles are large regions of the upper atmosphere that generally form during the night and tend to drift eastward after formation. Plasma bubbles can be thousands of kilometers north to south, hundreds of kilometers east to west, and thousands of kilometers in altitude. The composition and small structures along walls of plasma bubbles can interfere with radio waves such as GPS. The current work develops a method, analyzes 4 years of GOLD data, and generates a database of all plasma bubbles in GOLD's purview. Seasonal variations in occurrence of plasma bubbles is verified: highest during December solstice and lowest during June solstice. A slight increase in plasma bubble occurrence from year to year coincides with increases in solar activity. Little variation can be seen for plasma bubble drifts or inter-bubble separations by season and/or region.

1 Introduction

Ionospheric plasma bubbles (PBs) are regions of the ionosphere with irregular and sharp density gradients compared to the surrounding plasma. PBs form around lower geomagnetic latitudes within the upper thermosphere/ionosphere region (TI) during post-sunset hours and have a distinct optical signature (e.g. Weber et al. (1978); Ledvina and Makela (2005); Eastes et al. (2019). PBs are characterized by sharp density gradients: often more than two orders of magnitude relative to background plasma density (Magdaleno et al., 2017). Density gradients and small scale structures therein cause ionospheric scintillation, interrupting GPS and other trans-ionospheric radio waves (Hysell, 2000; Makela et al., 2006; Wan et al., 2018). This is of interest to researchers and industry alike.

PBs form from collisional and inertial instabilities (e.g. electromagnetic Rayleigh-Taylor and gradient-drift) (Ott, 1978). Vertical perturbations of low-density bottomside F-region plasma about the magnetic equator are believed to seed instabilities wherein depleted plasma propagates upwards. Vertical perturbations can be caused by gravity waves, tidal/vertical/shear winds, and vertical $\mathbf{E} \times \mathbf{B}$ plasma drifts (Sekar et al., 1995; Keskinen & Vadas, 2009; Vadas & Keskinen, 2010). Two-dimensional (e.g. Zargham and

Seyler (1989)) and three-dimensional (e.g. Keskinen et al. (2003); Huba et al. (2008)) simulations validate possible seeding mechanisms and show PB formation vertically, latitudinally, and longitudinally. Further refinements to these models (e.g. Yokoyama et al. (2014)) and comparisons with data (e.g. Aveiro et al. (2011)) continue to reveal the underlying physics, formation, and behavior of PBs.

PBs tend to align with local geomagnetic field lines and are narrower along magnetic longitudes, ranging from several to hundreds of kilometers, and will stretch along magnetic latitudes for thousands of kilometers (Immel et al., 2003). These structures also rise and stretch from the lower F-region of the ionosphere to well over 1000 km (Comberiate & Paxton, 2010). PB drifts are generally west to east with the background zonal plasma drift (Fejer et al., 1991; Makela, 2006; England & Immel, 2012; Liu et al., 2013). These regions of depleted plasma tend to have a decreasing velocity as we trace them upward in altitude which causes a perceived westward tilt (Aa et al., 2020). Variations in drift speeds along magnetic latitudes can lead to PBs taking a C or reversed C-shape (Mendillo & Tyler, 1983; Liu et al., 2013); however, this has also been attributed to neutral zonal winds at F-region altitudes (Anderson & Mendillo, 1983; Martinis et al., 2003). The observations required to develop an understanding of PBs comes from remote sensing and in-situ devices. Ground-based airglow and radar provide bottom side information, in-situ measurements provide data within and without, and global GPS TEC data allow continuous viewing of PBs.

Large scale statistical analysis can help provide an understanding of the seasonality, frequency, and general behavior of PBs during various periods of the solar cycle. Studies from Gentile et al. (2006), Huang and Roddy (2016), and Wan et al. (2018) have looked at data from 1989–2004, 2008–2014, and 2013–2017, respectively, to look at PB occurrence rates, drift speeds, and amplitudes as functions of year, month, local time, season, longitude, latitude, F10.7, DsT, and K_p. The current study further develops this understanding using Global-Scale Observations of the Limb and Disk (GOLD) 135.6 nm airglow nightside data. An automated method is developed to process GOLD data and detect PBs therein using a detrending scheme developed by Pradipta et al. (2015) to generate a database of PB occurrences. From there, a methodology is defined and used to identify PBs from one GOLD image scan to the next for drift speeds to be calculated. Unique PBs are defined and counted if used to calculate a drift speed. These PBs are also used to calculate interbubble separations. PB detections are analyzed by season and geographic regions. Analysis of PB drift speeds and separations by geographic region, magnetic region, and season provide a view of PB behavior within GOLD's view.

2 GOLD Mission and Data

The GOLD mission has a unique perspective on Earth's TI from its vantage point in geostationary orbit (GEO) above 0° latitude and −47.5° longitude. This provides GOLD with consistent data on the spatial and temporal evolution of the dayside and nightside TI over the American, Atlantic, and west African regions simultaneously via routine observations of the Earth limb and disk (Eastes et al., 2017, 2019). The GOLD imager consists of two identical and independent channels that can operate individually or simultaneously to collect 132–162 nm emissions from the TI by scanning across the disk and/or limb at regular intervals as little as 15–30 minutes, dependent on operations. Information on the temperature and composition of the TI system can be gleaned from these measurements and allow for the separation of temporal and spatial variations due to the consistent nature of the observations (Eastes et al., 2017). Nightside data is used to observe variations in radiance given off by radiative recombination of O^+ with electrons. These variations correspond to structures in the low magnetic latitudes such as the EIA and PBs (Eastes et al., 2019, 2020). Nightside scans start east of the dayside terminator along the eastern edge of the Earth disk and progress westward following the terminator with alternating north and south scans with a temporal cadence of ∼15 min. Scans

are taken simultaneously with both channels later in the evening. Each pixel within a scan has a spatial resolution of ∼95 km at nadir, ∼112 km nearer the limb, and are ill-defined at the limb (Eastes et al., 2017, 2020; McClintock et al., 2020).

The automated PB detection and tracking algorithm is implemented on data from October 5, 2018 to September 30, 2022 for statistical significance. Nightside (NI1) level 1C (L1C) data is used which contains geographic coordinates for corrected photon particle counts and calibrated radiance values. The latest version of L1C NI1 data is used. Scan cadence has varied throughout the mission with the advent of special operations and changing mission parameters. The method has therefore been designed to operate effectively with varied frequency of data.

3 Plasma Bubble Detection and Database Generation

3.1 Method Outline

The method for identifying the locations and characteristics of PBs in GOLD images has the following major steps:

1. Data are interpolated onto a regular grid in quasi-dipole coordinates to identify and later track features about the magnetic equator (3.2–3.4).
2. Individual north and south scans are combined into full images and the region of interest is isolated (3.5–3.6).
3. PBs are isolated from the background ionosphere and their properties including location, width, and intensity are recorded (3.7–3.11).

3.2 Cubic Spline Interpolation

The airglow data from GOLD is in a coarse irregular spatial grid in geographic co-ordinates, but the method requires data to be in a regular grid in quasi-dipole coordinates. This necessitates a two dimensional interpolation in array space for the nearest neighbor interpolation that follows. A simple two dimensional clamped cubic spline is implemented to accomplish this. Figure 1 shows the location of the original data points and the new interpolants. The number of interpolants between data points in array space is defined by a scale value: ten is used for this research. The effects of scaling on data can also be seen in figure 1.

3.3 Nearest Neighbor Interpolation

Nearest neighbor interpolation (NNI) is implemented for its simplicity and robust nature. This allows for simple transformation to a regular grid for analysis that comes later. NNI is done in half degree boxes with pixel centers at every half degree in longitude and latitude. The boundaries of NNI are shown in figure 1. Note the regions that would otherwise be void of data without the interpolants from the cubic spline. This NNI algorithm is implemented on each GOLD scan individually. Results of NNI are shown in figure 2a.

3.4 Quasi-Dipole Coordinate Conversion

PBs tend to follow the EIA and magnetic field lines; conversion to magnetic co-ordinates will significantly simplify the detection algorithm and analysis on the back-end. The magnetic coordinates used in this analysis are quasi-dipole (QD) coordinates, similar to that used by Karan et al. (2020). QD coordinates with a reference altitude of 300 km are selected because 135.6 nm airglow peaks near this region (Laundal & Richmond, 2017). Figure 2b shows the results of QD conversion.
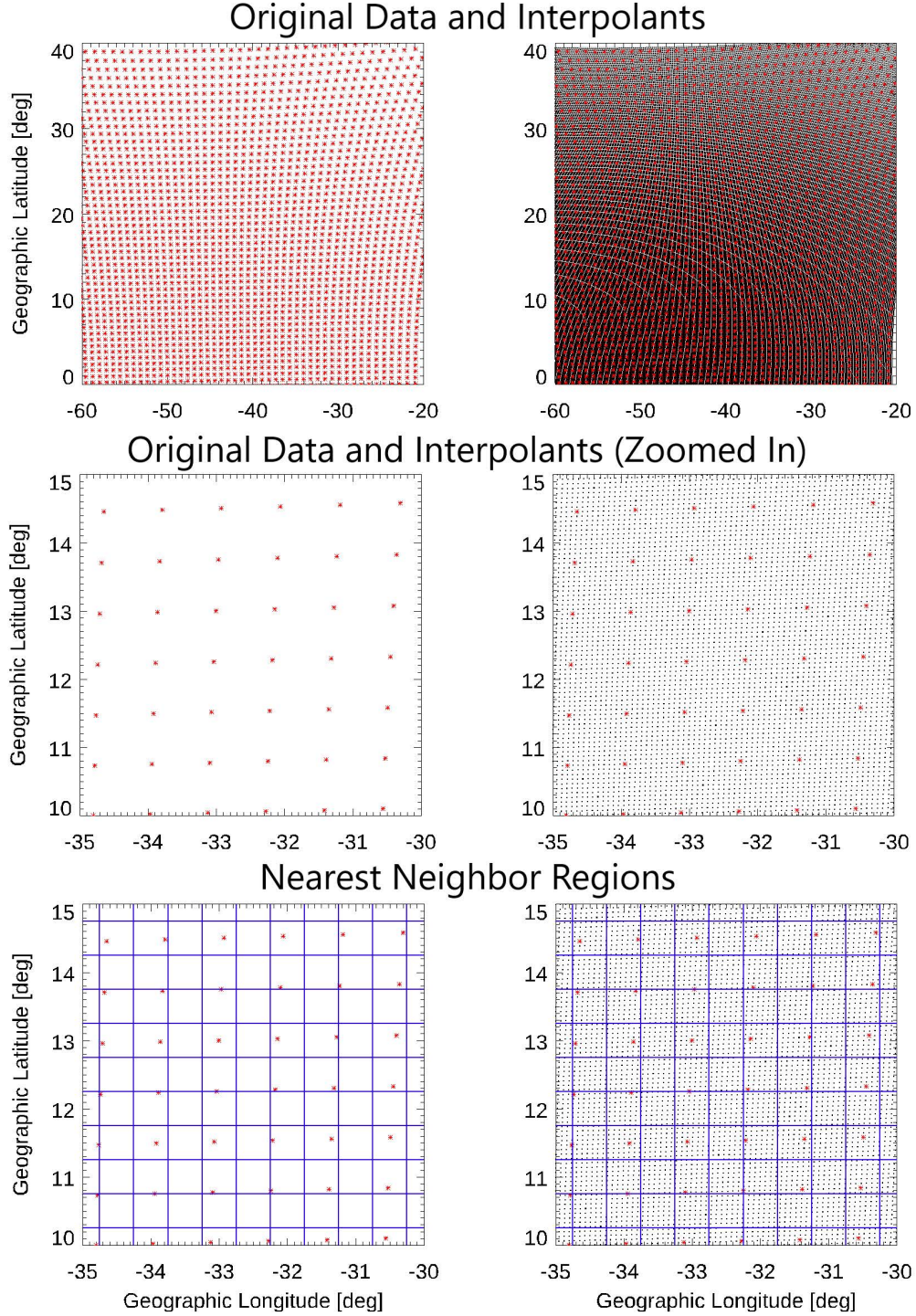
Original Data and Interpolants

Original Data and Interpolants (Zoomed In)

Nearest Neighbor Regions

Figure 1. Plots of GOLD data locations from November 28, 2018 at 2310 UTC in red (left column) and with interpolants overlaid in black (right column). Full view of data (top row), zoomed in (middle row), and nearest neighbor grid used for nearest neighbor interpolation (bottom row).
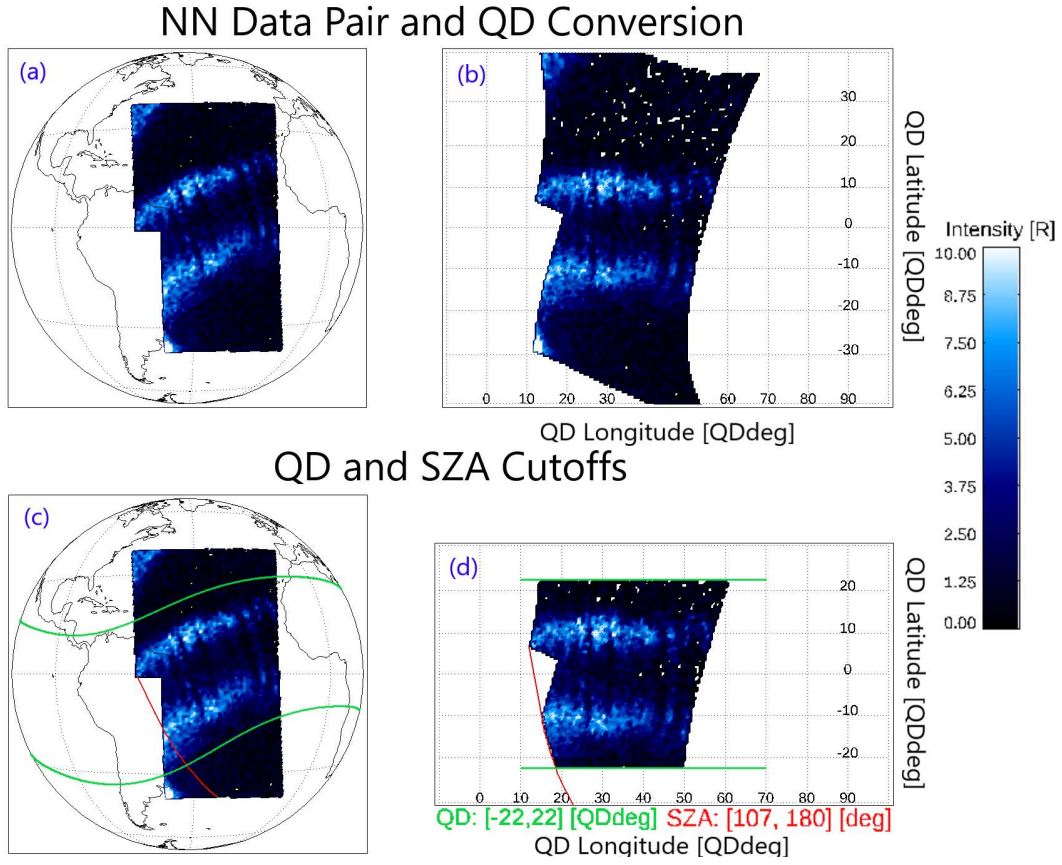
Figure 2. Paired north and south images after NNI (a) and QD conversion (b) for November 28, 2018 at 2310 UTC. SZA and QD cutoffs are displayed and implemented in (c) and (d), respectively.

3.5 Image Pairing

The GOLD imager consists of two identical and independent channels: A and B (Eastes et al., 2017). Either one or both channels are used for nightside Earth disk observations. When one channel is used, it will alternate scans of the northern and southern hemispheres with each integration period (Eastes et al., 2017). Conversely, both north and south scans can be done simultaneously when both channels are available. This necessitates the need to form images from pairs of scans to generate a continuous time series of the nightside ionosphere.

An example of the NNI, QD conversion, and data pairing for November 28, 2018 at 2310 UTC are shown in figure 2. Note how the EIA follow the magnetic equator northward and eastward in the region of the South Atlantic Anomaly (SAA) leading to a positive slope (latitude/longitude) from west to east and how this is translated to a slope of approximately 0 (QDlatitude/QDlongitude) in QD coordinates.

The first scan of the night is referred to as t_0, the second referred to as t_1, up to t_{i-1} for the last scan of the night where i is the number of scans for a given night. The first scan pair will then have time steps t_0 and t_1, the second uses t_1 and t_2, up to the final pair of t_{i-2} and t_{i-1}. This will generate up to $i-1$ scan pairs as subsequent north-north or south-south pairings are ignored. When looking at scan pairs, the earlier of the time steps will be referred to as t_0 and the later as t_1. This is for convenience and to acknowledge both scans are at different times and scan regions.

3.6 Isolating the Region of Interest

A minimum solar zenith angle (SZA) is implemented to prevent any dayglow and early evening data effected by the solar terminator from creeping into the data analyzed. This ensures only steady state nightside data is utilized. The minimum SZA cutoff value is calculated using the following equation,

$$\theta_{\mathsf{max}} = 90° + \mathsf{arccos}\Big(\frac{R_{\mathsf{Earth}}}{R_{\mathsf{Earth}} + A}\Big), \tag{1}$$

where θ_{max} is the maximum SZA in degrees, A is altitude, and R_{Earth} is Earth's radius with the later two in kilometers. It can be shown through spherical trigonometry that $\theta_{\mathsf{max}} = 90°$ on the surface of the Earth ($A = 0$) and that an increase in altitude increases θ_{max}. Note that (1) assumes ideal parallel light rays through all possible layers of the atmosphere and ionosphere and ignores refraction or scattering. Dayglow from oxygen (135.6 nm) is brightest below 200 km (Meier, 1991). Using 6378 km for Earth's radius and 200 km in (1) yields a SZA of $\theta_{\mathsf{max}} \approx 104$ deg. Using 135.6 nm nightglow altitude of 300 km yields $\theta_{\mathsf{max}} \approx 107$ deg. A minimum SZA of 107 deg is used as the cutoff to ensure no effects on nightside airglow from bottomside dayglow or solar terminator effects at 300 km. Figure 2c contains a bright spot in the southwest region due to the solar terminator. This bright spot is removed with the implementation of the SZA cutoff shown in red.

Occasional polar effects, such as aurora, can be viewed through nightside disk scans. QD cutoffs of ±22 QDdeg latitude are implemented to isolate the low latitude region of interest for PB detection. The SZA and QD cutoffs are shown in figure 2. Note the two bright regions in the north-west and south-west extents of the geographic image of figure 2 that are removed in the QD conversion. These bright regions could potentially lead to false EIA tracking and false PB detections.

3.7 Rolling Barrel Average for Detrending

GOLD sees PBs as dips in the brightness of 135.6 nm airglow which can be seen in figure 2 (Eastes et al., 2017). These dips in brightness are most clearly seen within

207   the EIA and magnetic equatorial trough (Karan et al., 2020). A detrending process is
208   used to highlight dips in brightness by way of a difference image which will correlate with
209   the PB locations. The averaging method used for detrending is referred to as a rolling
210   barrel average (RBAVG) because it simulates a barrel of some radius rolling over data
211   like a surface. This technique was developed for the detection of ionospheric anomalies
212   by Pradipta et al. (2015) and implemented on TEC data. This study applies it to non-
213   TEC data for the first time. This detrending method was chosen to maintain the integrity
214   of the data being detrended without the need for further corrections: local or otherwise.
215   Common detrending techniques, such as simple smoothing, stretch or skew structures
216   of interest and lead to potential false negatives.

217   The premise of the RBAVG is a barrel with sufficiently large radius will necessar-
218   ily 'roll over' dips in data, which can correlate to structures of interest. Specifics of the
219   geometry are shown in figure 3.
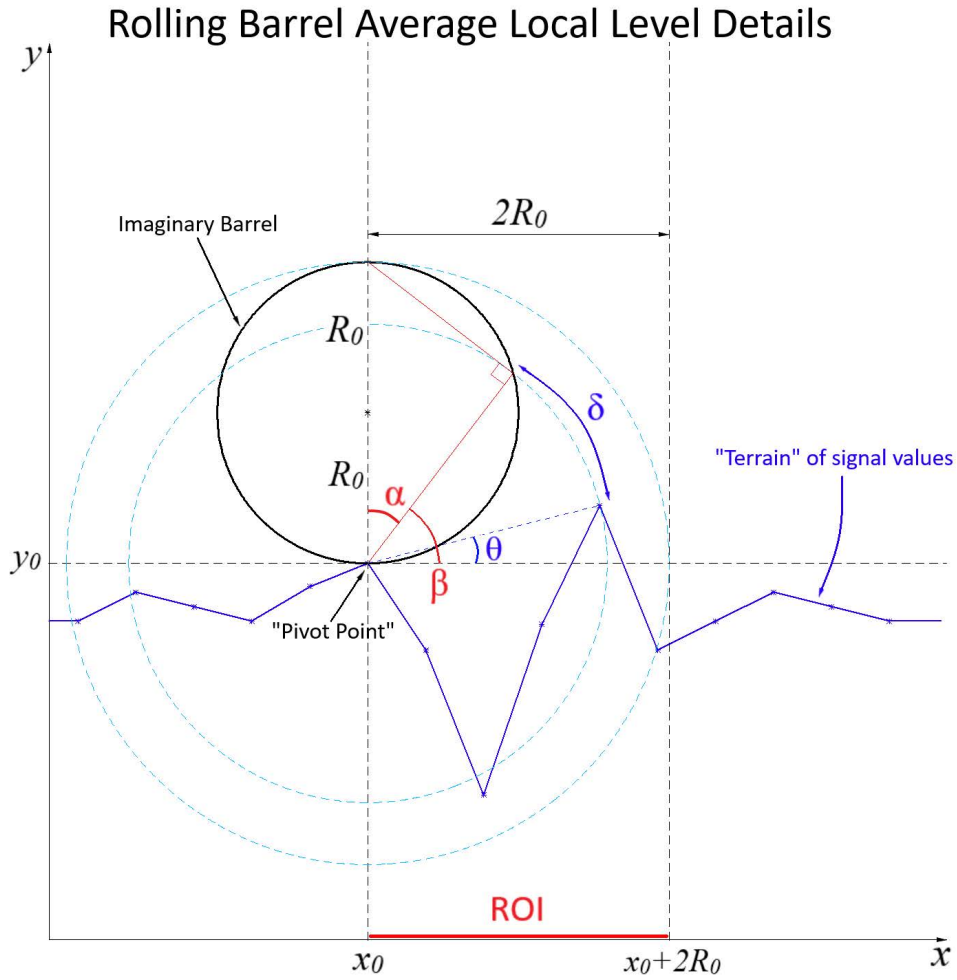
Figure 3. Rolling barrel average details and geometry. The pivot point is the current location of the barrel at (x_0, y_0), R_0 is the barrel radius, the region of interest (ROI) consists of all points the barrel could potentially 'roll' over, the angles α, β, and θ are used to derive δ for each point within the ROI (refer to Pradipta et al. (2015) for further details on these angles). Adapted from Pradipta et al. (2015).

Following Pradipta et al. (2015), at any given data point, RBAVG looks ahead to all data points along the region of interest (ROI) and calculates the δ for every point therein. This δ is the angular distance between the points on the barrel that would roll over a given data point within the ROI (see figure 3). The data point with the minimum δ is taken as the next pivot point (PP). This process assumes an ordered, not necessarily regular, domain. The data point ahead of the current PP is taken as the next PP if no data points are within the ROI which contrasts from Pradipta et al. (2015) taking the closest point outside of the ROI as the next PP. This is done to prevent skipping of data within an ROI due to noise or coarseness of input data. Once all PPs have been defined, a simple linear interpolation is implemented from one PP to the next. The curve generated is the detrended data.

Figure 4 shows a smoothing average and RBAVG implemented on a simple sine function. The smoothing average, window of 1.5π, requires a shift by a constant to match the data. More complex data with varying peaks and valleys would necessitate more localized corrections. The RBAVG, with $R_0 = 1.5\pi$ as defined in figure 3, follows the sine curve perfectly while skipping over gaps.

The detrended data are differenced with the input data to generate the red curves in 4. Note how the peaks and gradients of the difference data in regions of depletions are more pronounced with the RBAVG example compared to the smoothing example.

The bottom of figure 4 shows an example of RBAVG implemented on data from figure 2 along constant QDlatitude of 10 QDdeg with $R_0 = 4$ QDdeg. Note the three largest peaks of the difference image at 27, 32, and 44.5 QDdeg longitude and the bubbles that can be seen in the same regions of figure 2. The RBAVG implemented on data from 2 and the resulting difference data are shown in figure 5.

3.8 Equatorial Ionization Anomaly Crest Detection

As PBs are visible in the EIA and equatorward, EIA tracking ensures the algorithm does not search excessively north or south in QD coordinates when looking for PBs. EIA detection takes advantage of the fact that a meridional cross-section of the cropped EIA generally appears Gaussian-like in the magnetic north and south. Data is cropped from the magnetic equator to the northern (southern) QDlatitude cutoff defined previously and west to east by 5.5 QDdeg centered about each QDlongitude. This width in QDlongitude is comparable to the widths of PBs and would ensure the EIA detection is not heavily skewed by their presence. A boxcar smooth is implemented within each box along lines of QDlatitude and followed by a Gaussian fit along QDlongitude: shown in figure 5c and 5d. The bottom row of figure 5 show the EIA tracked in this manner in orange over QD data and the difference data. EIA detection and difference data are the basis for PB detection.

3.9 Plasma Bubble Detection

A single row of data is not sufficient to accurately determine what is a PB in a given region due to the signal to noise level (see figure 4). Implementing summations along QDlatitudes can highlight bright spots within difference data, which correspond to features aligned with the geomagnetic field. Difference image sums are taken over the EIA peak and 4.5 QDdeg magnetically equatorward. Additionally, summation along the magnetic equator are taken from -4 to +4 QDdeg latitude. This yields three regions of PB locations: northern EIA, southern EIA, and magnetic equator. The increased range for equatorial summation is to compensate for generally less intense nightglow along the magnetic equator. The QD northern, equatorial, and southern summation regions and the resulting southern sums are shown on figure 6.
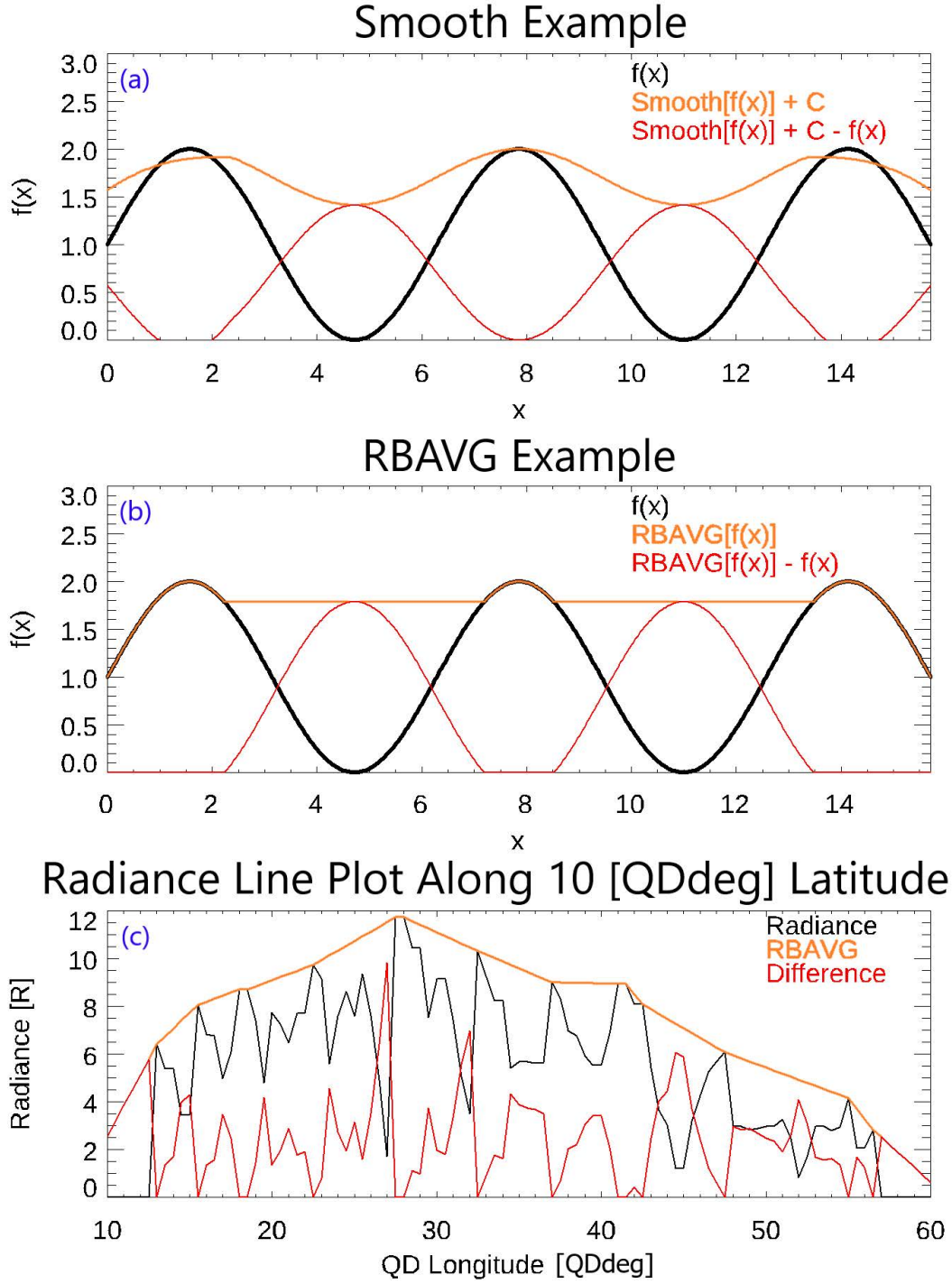
Smooth Example

RBAVG Example

Radiance Line Plot Along 10 [QDdeg] Latitude

Figure 4. Simple smoothing and rolling barrel average implemented on a sine function shifted up by 1 (a − b) and the rolling barrel average implemented on data from figure 2 along constant QDlatitude of 10 QDdeg (c). Smoothing window is 1.5π with $C \approx 0.707$, R_0 in (b) is 1.5π, and R_0 for bottom image is 4 QDdeg. Data is black, detrended data is orange, and difference data is red.
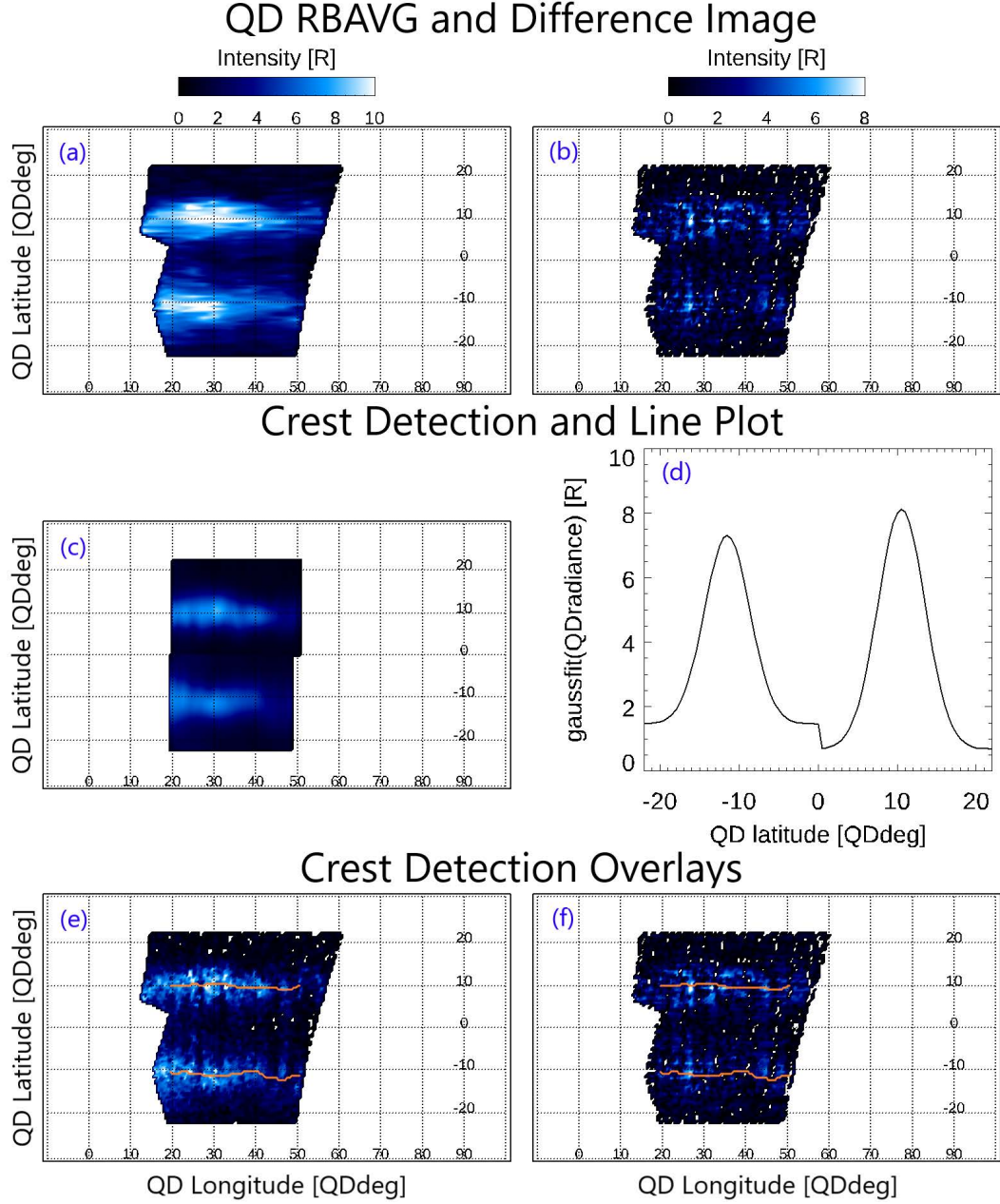
QD RBAVG and Difference Image

Crest Detection and Line Plot

Crest Detection Overlays

Figure 5. RBAVG data (a), difference data (b), smoothing Gaussian fit (c), Gaussian fit line plot along QDlongitude 30 QDdeg (d), QD data (e), and difference data (f) with detected EIA overlaid in orange: data from figure 2.

QD Difference Summation Regions

Southern Sums: Raw and Filtered

Southern Uncertainty Analysis
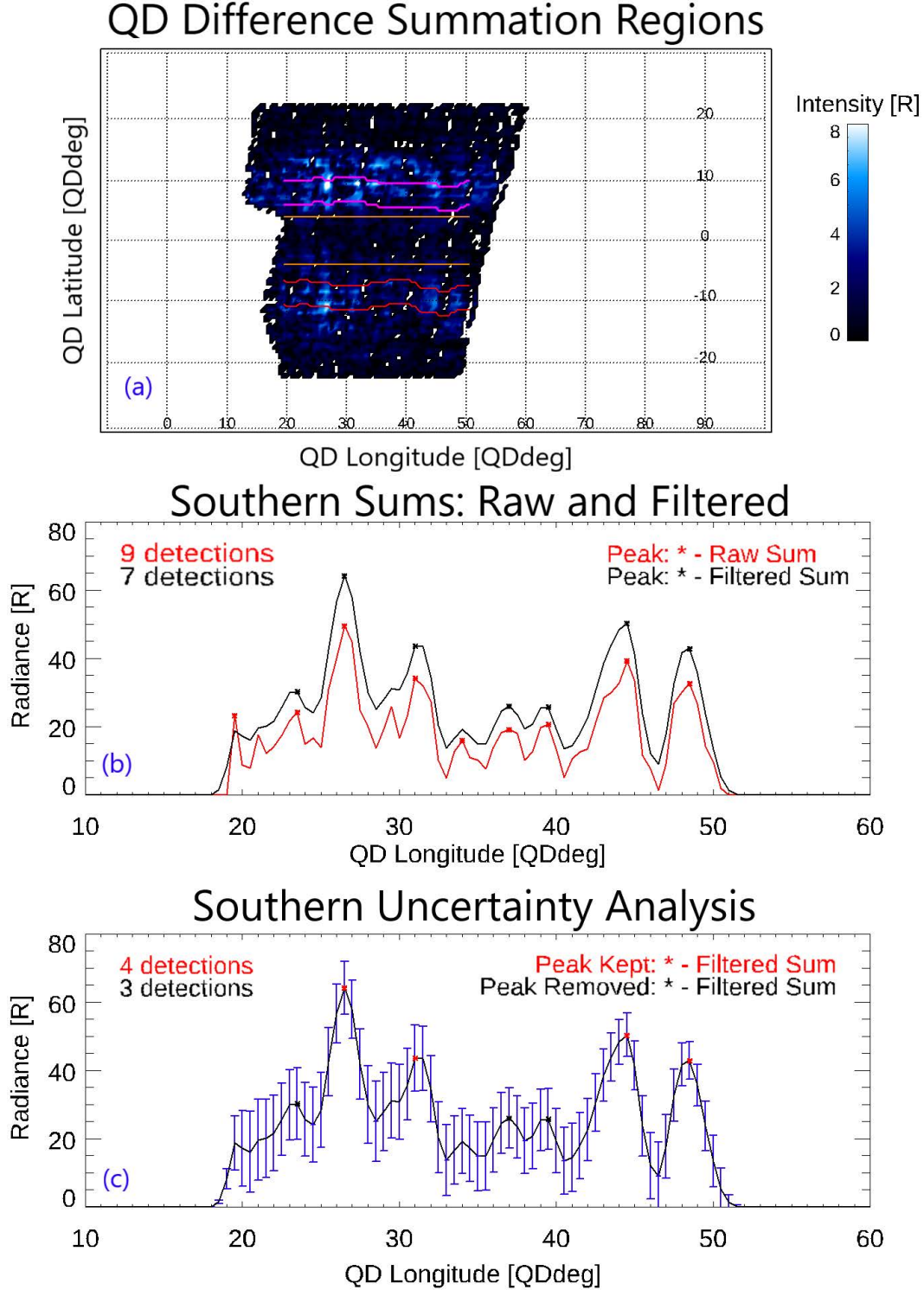
Figure 6. QD data with summation regions marked in magenta, orange, and red for the northern EIA, magnetic equator, and southern EIA, respectively (a), raw and filtered sums in red and black, respectively (b), and uncertainty analysis (c). Uncertainties about each QDlongitude are $\pm 1.5\sigma$ and marked in blue with valid/invalid detections in red/black.

The sums are run through a 2.5 QDdeg wide triangular convolution filter. Filtering in this manner smooths regions around shallow peaks and prevents double counting PBs. A simple peak detection algorithm then picks out potential PB locations. Each point is compared to all points 1.5 QDdeg west and east of itself. If it is larger than all other values, it is a peak, else it is not. Similarly, all minimum values between peaks are picked out as valleys. The results of the peak detection on both the raw sums and filtered sums for the southern region are shown on figure 6.

Uncertainty analysis provides the final protection against false positive detections. Both systematic and random uncertainties from the L1C data files have been propagated throughout the process. The summation in quadrature of these uncertainties are used as the measure of uncertainty: σ. Peak uncertainties are compared to the closest valley uncertainties to the east and west. If a peak less its 1.5σ is less than both valleys plus their respective 1.5σ values, then the peak is considered too shallow and not a PB detection. If a peak lies on the edge of the data, it is compared to the closest valley. 1.5σ is used as this is effectively a 3σ uncertainty filter. Note the PB detections and rejections on the bottom of figure 6. The western most and two detections between 35 and 40 QDdeg longitude have been deemed too uncertain to be PBs when compared to the relevant valleys. Two detections at 26.5 and 44.5 QDdeg longitude are well within uncertainty bounds on either side. A detection at 31 QDdeg longitude fails the uncertainty check to the west, but passes to the east and is kept. The eastern most detection only has a valley to the west of itself and passes its single uncertainty check.

The NNI data lead to PBs that are detected on 0.5 QDlongitude grid. To identify the location of the center of each PB, Gaussian fits are applied to each detection using QDlongitudes 1.5 degrees to the east and west. The peak location of the resulting Gaussian is taken as the final QDlongitude for a given detection (figure 7). Note how each Gaussian lies within the domain of its respective detected peak. The final results of the detection algorithm in QD coordinates and geographic coordinate conversions are shown in figure 7. EIA crest locations are used as the northern and southern PB QDlatitudes and all PBs detected along the magnetic equator are assumed to be at 0 QDdeg latitude for simplicity.

3.10 Determination of Plasma Bubble Width

The last thing determined before generating the final database is a measure of PB widths. The first location to the magnetic east and west of each PB lesser or equal 75% of the detected peak filtered sum are defined as the full width at 75% max. These are generated such that the eastern less the western 75% provides a measure of PB width that can be quantified and analyzed. The value of 75% is chosen as anything less than 75% leads to PB width extents that overlap with neighboring PBs whereas greater than 75% leads to ill-defined and false reported widths.

Note that these measures of width are most ideal when PBs follow lines of constant magnetic longitudes due to the summation along QDlatitudes (section 3.9). The widths will be overestimated should the PBs take on a C-shape or reversed C-shape as shown in Mendillo and Tyler (1983) and Liu et al. (2013).

3.11 Database Generation

The following values are saved for a given image pair for each PB once all bubbles have been classified for each magnetic region; Gaussian coefficients for PB center location, QDlongitude and latitude, year, day of year (DoY), UTC for both scans that comprise an image, intensity sum and filter values, random and systematic uncertainties pre and post convolution filter, western and eastern 75% max measures of width, and each
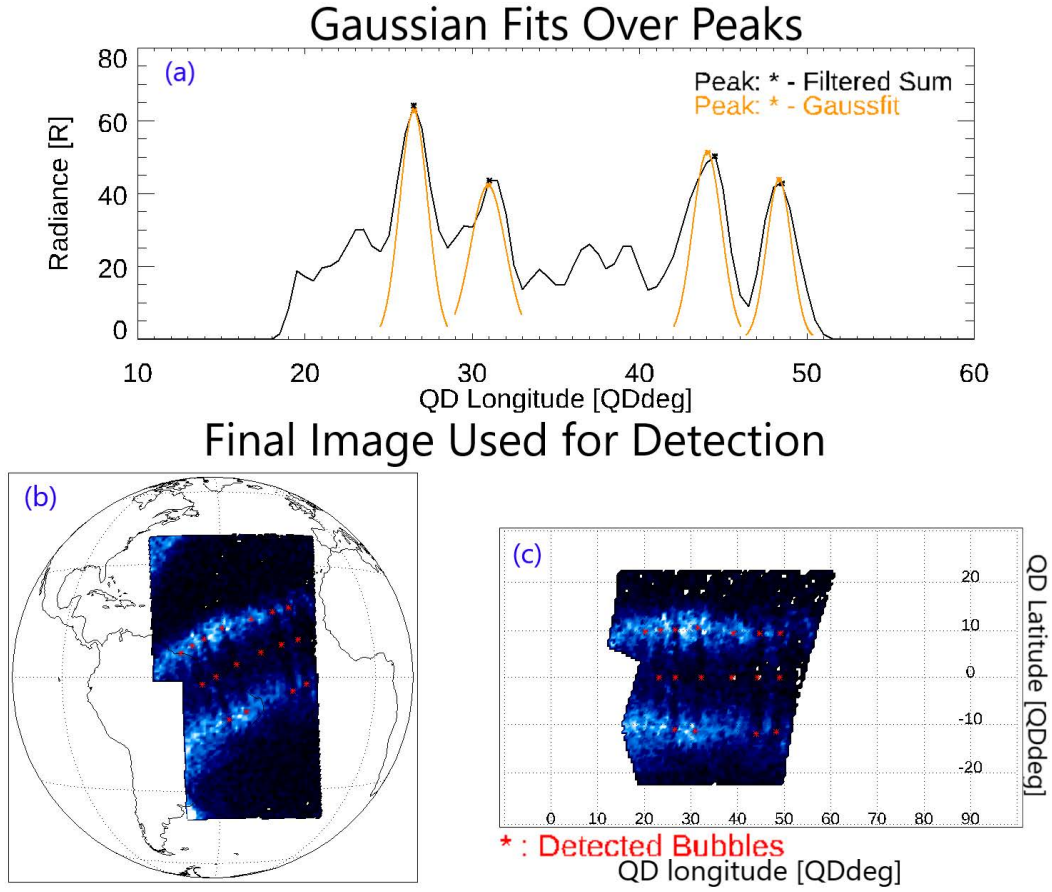
Figure 7. Filtered sums with Gaussian fits of peaks overlaid in orange (a) and detected PBs marked in red on GOLD disk image pair and QD conversion (b – c).

individual image's geographic scan region: north or south, SZA, and the intensity of crest locations. The full 4 years is available, see open research statement.

4 Selection, Drifts, Counting, and Separation

Two things prevent accurate drift calculations of PBs. Firstly, GOLD images can share a north or south scan from one image to the next leading to a single double count at best: multiple double counts at worst. Second, there is no definitive way to show a given PB is the same one image to the next. The first is simple to check for. Various approaches have been used for the second and are dependent on the data-set.

S. H. Park et al. (2007) took advantage of IMAGE-FUV's low temporal cadence compared to the motion of PBs (approximately 2 minutes) to detect PB locations and drift velocities by looking at keograms to develop their automated PB detection algorithm and calculate PB drift speeds with low spatial resolution: ~100 km at nadir at apoapsis (Mende et al., 2000). Huang and Roddy (2016) used 6 years of high resolution in-situ data from C/NOFS with a temporal cadence dependent on its orbital period of ~100 minutes to identify individual substructures within each PB and calculate drifts. GOLD's nightside data lies somewhere in the middle. From section 2, the nightside scans have a temporal cadence of ~20 minutes with more frequent scans in recent data products and a spatial resolution of ~ 95 km at nadir (McClintock et al., 2020). This temporal cadence allows for consistent and more frequent tracking of bubbles from one scan to the next with less uncertainty within the same night and does so from a fixed vantage point.

Karan et al. (2020) showed how GOLD's nightside data could be used to detect, track, and calculate drifts of PBs by manually selecting and analyzing dips in radiance which correlate with regions of depleted plasma. S. H. Park et al. (2007) and Huang and Roddy (2016) showed the power in implementing an automated method for detection, analysis, and statistics regardless of data.

The automated process implemented for this research and the relevant sections are as follows:

1. PBs are selected from distinct images (4.1).
2. Drifts are calculated from one image to the next (4.2).
3. PBs are counted (4.3).
4. Double counts removed (4.4).
5. PB separations are calculated (4.5).
6. Uncertainty calculations used (4.6).

4.1 Plasma Bubble Selection

Comparing one image's PBs with the next image's PBs must be done to calculate PB drifts and counts. Care must be taken not to compare the same scan with itself from one image to the next as can be seen in figure 8. All southern region PBs would be compared with themselves if image 8a were compared with image 8b as both have the same southern scan. Comparing image 8a with image 8c would ensure unique scans in both images. The same logic can be applied if the current image were instead 8b. This is accomplished as follows.

The current image, Img_n, is selected from the database by looking at all PBs on a given year, year_n; DoY, DoY_n; and time pair $(t_{0,n}, t_{1,n})$ in UTC where n is the image index and starts at zero. It follows the next image will be Img_{n+1}. A check is implemented to verify that $t_{0,n} > t_{0,n+1}$, $t_{0,n} > t_{1,n+1}$, $t_{1,n} > t_{0,n+1}$, and $t_{1,n} > t_{1,n+1}$. If any of these are not true, then the next image is taken and a comparison of Img_n and Img_{n+2}

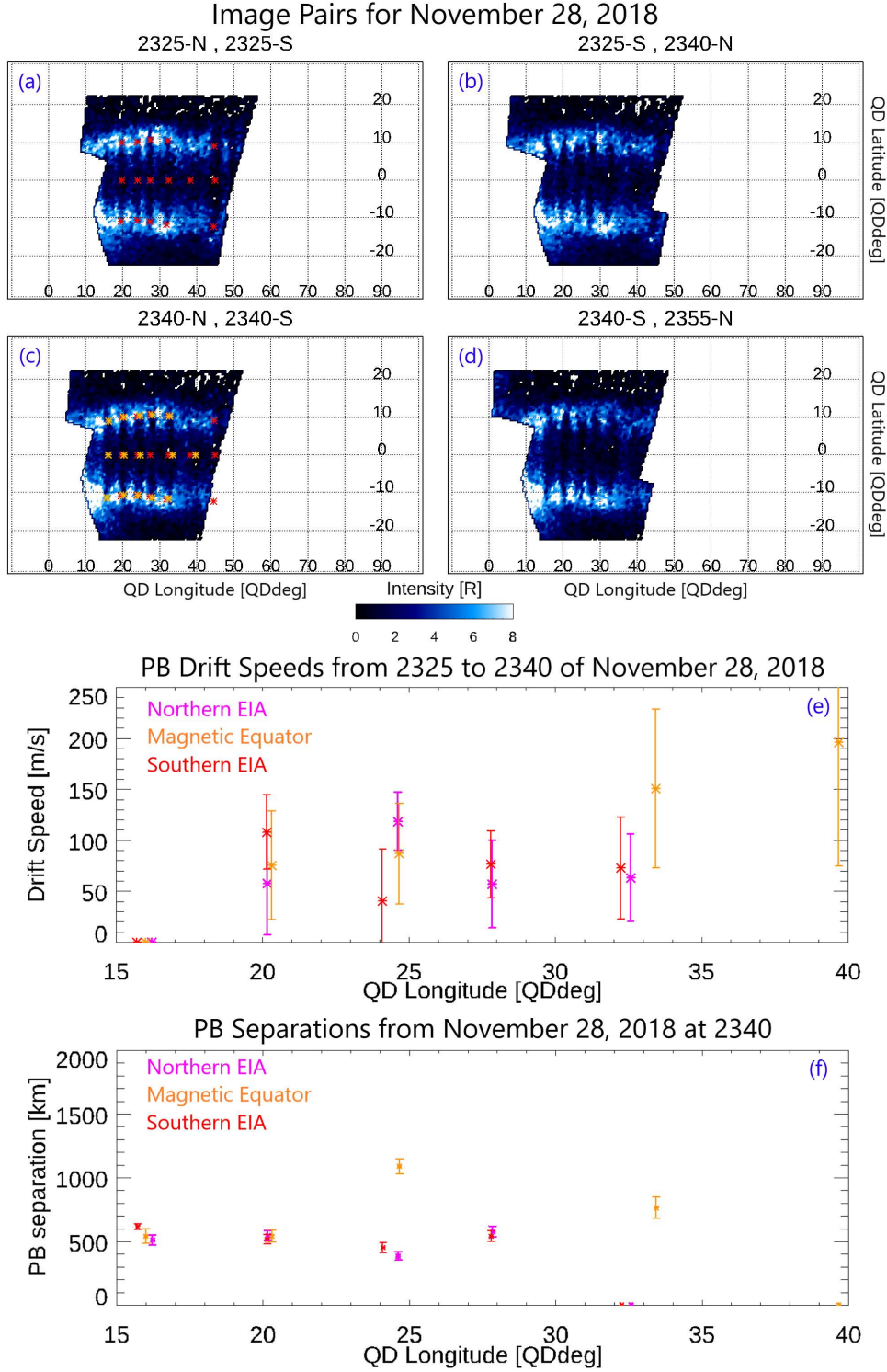## Image Pairs for November 28, 2018

Figure 8. Image pairs in QD coordinates for November 28, 2018 in order: (a), (b), (c), and (d). Time steps and scan region for pairing are shown above each image as t_0-N/S , t_1-N/S pairs (N: north, S: south). PBs are marked in (a) and (b) in red and orange, respectively. Image (a) PBs are overlaid (c). Plot (e) shows drift speeds as calculated from image (a) to (c) in meters per second while plot (f) shows PB separations from image (c). Values are plotted with respect to QDlongitude for quick reference to the PBs marked above. Error bars are 1 sigma uncertainties derived in section 4.6.

times are done. This process is repeated until the inequalities are true. Magnetic regions are processed independently. Img_n and Img_{n+1} will be used henceforth for simplicity.

Every Img_n will therefore have at least one PB, $\mathsf{PB}_{i,n}$, where i is the bubble index within image n and also starts at zero. PB indices start at the western most region of a given image and move eastward as i increases. Using this notation for the northern regions of figure 8 would yield Img_0 and Img_1 for 8a and 8c, respectively. The westernmost PBs for 8a and 8c would be, respectively, $\mathsf{PB}_{0,0}$ and $\mathsf{PB}_{0,1}$. The PBs east of these would be $\mathsf{PB}_{1,0}$ and $\mathsf{PB}_{1,1}$ and so on.

4.2 Drift Calculation

PBs are tracked one at a time by comparing a single PB in one image with all PBs in the next image that lie slightly west and fully east of its last known position. This is done for each magnetic region individually. This method of tracking was chosen over a full image correlation analysis method for several reasons. PBs tend to drift magnetically east while GOLD scans move progressively westward with UTC with an integration period of $\sim$ 15 minutes. This leads to image comparison time differences of $\sim$15 – $\sim$60 minutes and regions that do not overlap with longitude. The cadence of scans that form the images also changes over the course of the GOLD mission for changing mission operations and special operations which can lead to more inconsistency with time differences from image to image. Features of interest are able to propagate, change shape, and disappear from view within this time. The large and varying time steps along with non-ideal overlap in longitude from image to image therefore does not lend itself to a full image correlation analysis which assumes drifts are largely consistent and features persist in a regular manner.

All PBs are initialized with a drift of zero. Drifts are calculated by comparing PBs from Img_n and Img_{n+1} in a QDwest to QDeast manner by magnetic region. This is done to take advantage of the generally eastward drift of nightside PBs (England & Immel, 2012; Huang & Roddy, 2016). $\mathsf{PB}_{i,n}$, is compared to all PBs from Img_{n+1} that lie up to 1.0 QDdeg west and all PBs east of $\mathsf{PB}_{i,n}$. The value of 1.0 QDdeg west was chosen to include some potential minimal westward drifts. The PB in Img_{n+1} that yields the minimum QDlongitude change relative to $\mathsf{PB}_{i,n}$, with further checks implemented later, is defined as the same PB and referred to as $\mathsf{PB}_{j,n+1}$. The currently set PBs of $\mathsf{PB}_{0,0}$ and $\mathsf{PB}_{0,1}$ from section 4.1 are defined similarly when applied to figure 8.

Distance and a time step are required to calculate drifts. The midpoint of both image's times are used,

$$\Delta t_{n+1} = \frac{t_{0,n+1} + t_{1,n+1}}{2} - \frac{t_{0,n} + t_{1,n}}{2}, \qquad (2)$$

where Δt_{n+1} is the time step from Img_n to Img_{n+1}.

A simple QD coordinate drift is calculated to determine the direction of the PB drift,

$$\theta_{j,n+1}^{\mathsf{QD}} = \frac{\mathsf{QDlon}_{j,n+1} - \mathsf{QDlon}_{i,n}}{\Delta t_{n+1}}, \qquad (3)$$

where $\theta_{j,n+1}^{\mathsf{QD}}$ is the QD coordinate drift in QD deg per hour with $\mathsf{QDlon}_{j,n+1}$ and $\mathsf{QDlon}_{i,n}$ being the QDlongitudes for $\mathsf{PB}_{j,n+1}$ and $\mathsf{PB}_{i,n}$, respectively. $\theta_{j,n+1}^{\mathsf{QD}}$ positive (negative) implies PB drift is eastward (westward).

Bubble QD coordinates are converted to geographic and arc length distances are calculated with a great circle calculation which takes slight variations in Earth's radius with latitude into account using the geographic coordinates for $\mathsf{PB}_{i,n}$ and $\mathsf{PB}_{j,n+1}$ as fol-

408   lows,

$$\theta_{j,n+1} = \cos^{-1}\Big(\sin\left(\mathsf{lat}_{i,n}\right)\sin\left(\mathsf{lat}_{j,n+1}\right) + \cos\left(\mathsf{lat}_{i,n}\right)\cos\left(\mathsf{lat}_{j,n+1}\right)\cos\left(\mathsf{lon}_{i,n} - \mathsf{lon}_{j,n+1}\right)\Big),$$

409   (4)

410   followed by,

$$d_{j,n+1} = \theta_{j,n+1}\left(R_{\mathsf{Earth}} + A\right), \tag{5}$$

412   where $\theta_{j,n+1}$ is the angle that subtends $\mathsf{PB}_{i,n}$ and $\mathsf{PB}_{j,n+1}$ in radians and $d_{j,n+1}$ is the
413   arc length between $\mathsf{PB}_{i,n}$ and $\mathsf{PB}_{j,n+1}$. The geographic coordinate terms for $\mathsf{PB}_{i,n}$ and
414     $\mathsf{PB}_{j,n+1}$ are $\mathsf{lat}_{i,n}$ and $\mathsf{lat}_{j,n+1}$ for latitudes and $\mathsf{lon}_{i,n}$ and $\mathsf{lon}_{j,n+1}$ for longitudes, respec-
415   tively.

416   The final drift magnitude is simply,

$$v_{j,n+1} = \frac{d_{j,n+1}}{\Delta t_{n+1}}, \tag{6}$$

418   where $v_{j,n+1}$ is positive eastward (negative westward) as determined by (3).

419   The highest previously noted drift speed is $\sim 8\frac{\deg}{\mathrm{hr}}$ by Mendillo and Baumgard-
420   ner (1982) and Sinha and Raizada (2000). Thus, a maximum drift check of $8\frac{\deg}{\mathrm{hr}}$ is im-
421   plemented. If,

$$\frac{\theta_{j,n+1}}{\Delta t_{n+1}} \times \frac{180°}{\pi} > 8\frac{\deg}{\mathrm{hr}}, \tag{7}$$

423   then $\mathsf{PB}_{i,n}$ and $\mathsf{PB}_{j,n+1}$ are deemed as unique PBs and $v_{j,n+1}$ is unchanged.

424   An example of these calculations are provided in figure 8e using image 8a as Img_0
425   and image 8c as Img_1. Note that a total of 5, 6, and 5 drifts are calculated for the north-
426   ern, equatorial, and southern regions, respectively, for Img_1 while there are 7, 6, and 4
427   PBs in the same QD regions in Img_0. The 3 new PBs in Img_1 (westernmost of the equa-
428   torial and southern regions) are assigned the default drift of zero at this stage. PBs with
429   drift values of zero that are not used to calculate a drift speed are not used in later anal-
430   ysis and are simply used to identify PBs seen only once.

431   It is important to note these drift calculations are taken from the EIA peaks at $\mathsf{PB}_{i,n}$'s
432   to $\mathsf{PB}_{j,n+1}$'s location as defined in section 3.9. Therefore, this method does not provide
433   information on gradients in PB velocity with respect to QDlatitude.

4.3 Plasma Bubble Counts

435   This method requires PBs to be seen in at least 2 images to be counted and tracked.
436   This ensures only PBs that persist longer than a single image integration period are counted.
437   All PBs are initialized as having a count number, c, of zero (uncounted) with,

$$\mathsf{PB}_{i,n}(\text{count}) = c_0, \tag{8}$$

439   where 'count' is an index value for the database accessing PB count numbers and $c_0 =$
440   0 is the initialized PB count value. PBs are counted in order of drift calculation as de-
441   fined in section 4.2.

442   If (7) is false, then a check on $\mathsf{PB}_{i,n}(\text{count})$ and $\mathsf{PB}_{j,n+1}(\text{count})$ is done and c val-
443   ues are updated as follows,

$$\mathsf{PB}_{i,n}(\text{count}) = \begin{cases} c_{\mathsf{max}} + 1 & , \ c = c_0 \\ c & , \ c \neq c_0 \end{cases} ; \ \mathsf{PB}_{j,n+1}(\text{count}) = \mathsf{PB}_{i,n}(\text{count}) \tag{9}$$

445   where c_{max} is the current max c value in the database thus far.

4.4 Double Count Removal

Removal of all double counts and unused PB occurrences is now trivial and occurs following drift calculations and count assignments. With all PBs labeled with count values greater or equal one, simply remove all PBs in the database that are still labeled as c_0.

4.5 Plasma Bubble Separation

Similar to prior sections, all PB separations are initialized as zero. Plasma bubble separation is calculated in QD and geographic coordinates by looking through all PBs in a single image as selected in section 4.1. Img_n will have PBs for $i = [0, \ldots, i_{\mathsf{max}}-1]$ where i_{max} is the total number of PBs in Img_n. From a QD west to east manner, $\mathsf{PB}_{i,n}$ is compared to $\mathsf{PB}_{i+1,n}$ for all i in Img_n.

If $i_{\mathsf{max}} > 1$, then separations are calculated as follows,

$$s_{i,n}^{\mathsf{QD}} = \mathsf{QDlon}_{i+1,n} - \mathsf{QDlon}_{i,n}, \tag{10}$$

$$s_{i,n}^{\mathsf{GEO}} = \cos^{-1}\Big(\sin\left(\mathsf{lat}_{i,n}\right)\sin\left(\mathsf{lat}_{i+1,n}\right) + \cos\left(\mathsf{lat}_{i,n}\right)\cos\left(\mathsf{lat}_{i+1,n}\right)\cos\left(\mathsf{lon}_{i,n} - \mathsf{lon}_{i+1,n}\right)\Big), \tag{11}$$

$$s_{i,n}^{\mathsf{km}} = s_{i,n}^{\mathsf{GEO}}\big(R_{\mathsf{Earth}} + A\big), \tag{12}$$

where $s_{i,n}^{\mathsf{QD}}$ is the QD coordinate separation in QDdeg, $s_{i,n}^{\mathsf{GEO}}$ is the angle that subtends $\mathsf{PB}_{i,n}$ and $\mathsf{PB}_{i+1,n}$ in radians and is similar to (4), and $s_{i,n}^{\mathsf{km}}$ is the PB separation in kilometers between $\mathsf{PB}_{i,n}$ and $\mathsf{PB}_{i+1,n}$.

It is worth noting that some separation values may be overestimated due to the removal of initial detections (3.9) and PBs with no associated drift speed (4.3 and 4.4). All results will be interpreted with this in mind.

4.6 Uncertainty Calculations

QD position uncertainties are calculated during section 3.9 and take summation uncertainties into account. QD coordinate uncertainties are added in quadrature from one PB to the next for both drift and separation calculations as follows,

$$v_{j,n+1}^{\mathsf{unc}} = \pm \frac{e \times \sqrt{(\mathsf{PB}_{i,n}^{\mathsf{unc}})^2 + (\mathsf{PB}_{j,n+1}^{\mathsf{unc}})^2}}{\Delta t_{n+1}}, \tag{13}$$

for $v_{j,n+1}$ uncertainty and,

$$s_{i,n}^{\mathsf{km,unc}} = \pm\, e \times \sqrt{(\mathsf{PB}_{i,n}^{\mathsf{unc}})^2 + (\mathsf{PB}_{i+1,n}^{\mathsf{unc}})^2}, \tag{14}$$

for $s_{i,n}^{\mathsf{km}}$ uncertainty such that,

$$e = \big(\frac{116}{1}\frac{\mathsf{km}}{\mathsf{GEOdeg}}\big) \div \big(\frac{1.05}{0.7071}\frac{\mathsf{QDdeg}}{\mathsf{GEOdeg}}\big). \tag{15}$$

$\mathsf{PB}^{\mathsf{unc}}$ values are relevant coordinate uncertainties in QDdeg and e is a conversion scalar with units $\frac{\mathsf{km}}{\mathsf{QDdeg}}$. The first term of e is the maximum nearest neighbor distance per its distance in degrees within the geographic region of interest. The second term of e is the minimum QD degree difference per geographic grid spacing during coordinate transformation. e is approximately $80\frac{\mathsf{km}}{\mathsf{QDdeg}}$ for the current work.

5 Results

The method developed in sections 3 and 4 are implemented on all the data from section 2 to create a single database of PBs. Generating a database grants ease of access and filtering for deeper analysis. Results are consolidated and shown as follows:

1. PB Detections (5.1),
2. Seasonal Variation of PB Counts (5.2),
3. PB Characteristics by Geographic Region (5.3),
4. PB Drift Speeds (5.4),
5. PB Widths and Separations (5.5).

5.1 Plasma Bubble Detections

Heat maps of individual PB detections are shown in figure 9. Total detections are highest during December solstice (November – February), lower during the September equinox (September and October) and March equinox (March and April), and lowest during June solstice (May – August). This is corroborated by the time series plots in the same figure. Detections during the December solstice and equinoxes are largely symmetric about northern and southern EIAs, but there exists an asymmetry within June solstice, especially over west Africa. This phenomenon is also visible in prior studies, such as J. Park et al. (2022). The phenomenon has been attributed to the sun's apparent location during the day and the solar terminator being nearly parallel to the QD field lines about the SAA. The spike in total detections during the 2022 solstices and equinoxes can be attributed to GOLD's change in mission operations and is accounted for by counting unique PBs in the next section.

5.2 Seasonal Variation of Plasma Bubble Counts

After accounting for unique PB detections (section 4.4), the spike in 2022 noticed prior is no longer evident in figure 9 Using unique PBs, GOLD sees a quasiperiodic behavior over the year and a slight general increase from 2018 – 2022 (figure 9). Comberiate and Paxton (2010) and Magdaleno et al. (2017) show consistent seasonal variations with GUVI data and GPS data, respectively, in similar geographic regions comparative to the time series plots of unique PB counts shown in figure 9. Further, the PB detections and counts exhibit quasiperiodic behavior. Rises in peak counts from December solstice to December solstice are also visible and may be due to increased solar activity as the solar cycle transitions from solar min towards solar max. Comberiate and Paxton (2010) show decreases in PB occurrences from 2002 to 2007 while Magdaleno et al. (2017) show a similar solar dependence; both corroborate these results.

5.3 Plasma Bubble Characteristics by Geographic Region

Geographic regions are defined to identify any variation in PB characteristics by location as follows: South American (SA), Atlantic (AT), and west African (AF) sectors from -90 to -34, -34 to -18, and -18 to 15 degrees longitude, respectively. The eastern and western limits are chosen arbitrarily outside of GOLD's view. The aforementioned regions were chosen as the geomagnetic equator has a sharp positive slope from east to west with QDlatitude over SA, shallower and decreasing slope over AT, and nearly zero slope over AF. Figures 10a and 10b show PB detections across the whole database and by season, respectively, by geographic region. More PB detections are visible to the west in figure 10a, but figure 10b shows this largely depends on season.

Martinis et al. (2021) looked at PB occurrence and formation with GOLD data during November 2018 and March 2019 in several geographic regions. They note higher occurrence rates in their West-American and Brazil-West Atlantic sectors, which coincide with the defined SA region, and lower occurrence rates in their East Atlantic-West-African sector, which coincide with the defined AF region. The December solstice heat map shows an overall agreement with Martinis et al. (2021)'s results over the entire database; however, the spring equinox heat map is less comparative with their March results. Overall, more PB activity occurs in the western region of GOLD's purview. This holds true
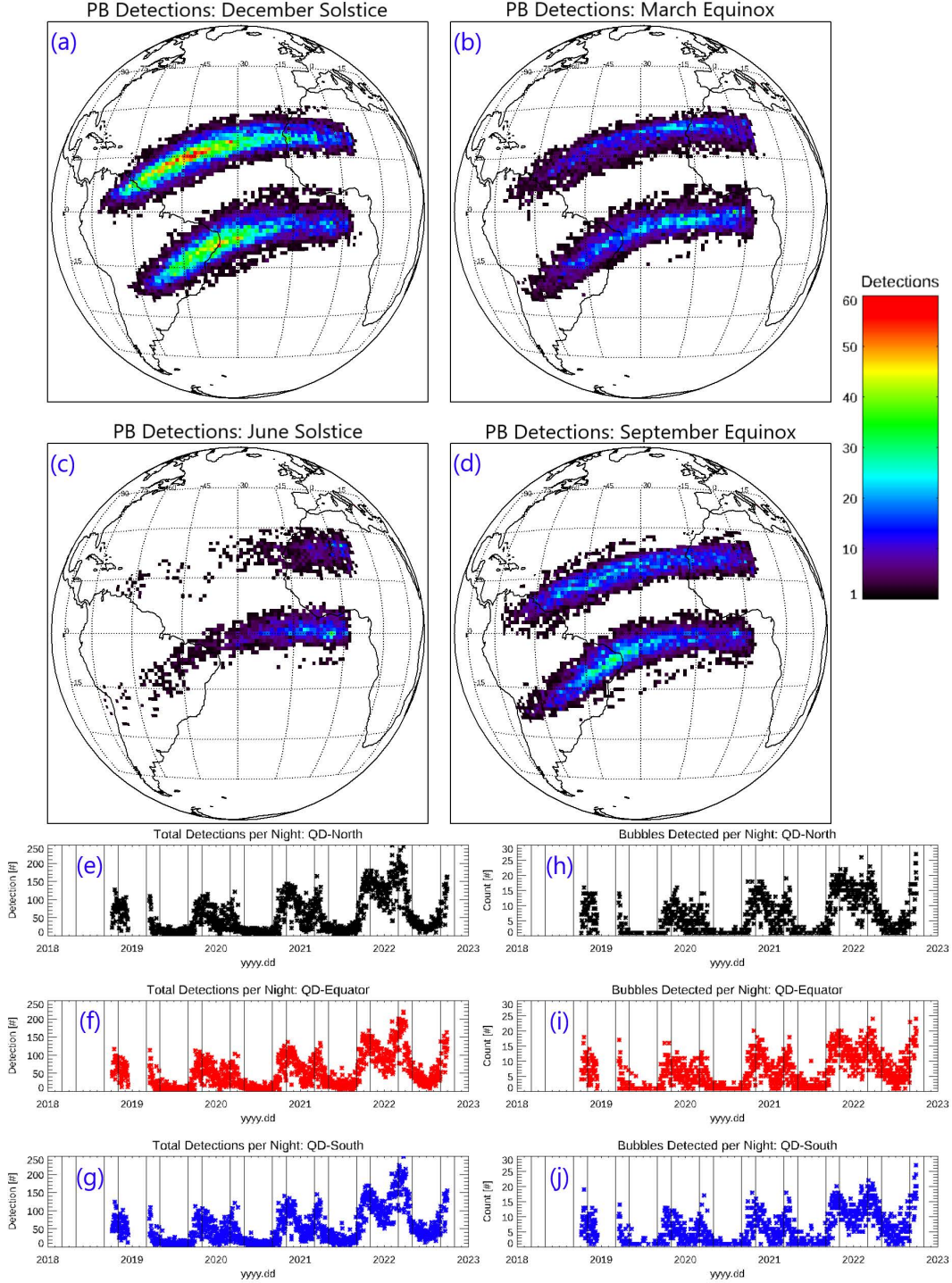
Figure 9. Total unique PB detection heat maps by season (a – d), total detections (e – g), and unique PB counts per night (h – j). The magnetic equator is not present in heat maps as all PBs detected in this region are assumed at the magnetic equator. Solstices and equinoxes have been demarcated by vertical lines for time series plots.

for December solstice and is in agreement with Martinis et al. (2021); however, spring equinox shows less variation. Looking at specific longitude regions used by Martinis et al. (2021) of -65° − -55°, -50° − -40°, and -10° − 0° yields opposite results of ∼5.8%, ∼16.6%, and ∼17.4% of total respectively. Note this difference could be caused by how Martinis et al. (2021) define occurrence rates, relative sample sizes used during analysis, or the day of year ranges used between studies.

5.4 Plasma Bubble Drift Speeds

Drift speed histograms are shown in figures 10 and 11. All histograms have similar shapes, means, medians, and peak locations, with the exception of drift speeds over SA during June solstice which has insufficient data points. While the breadth of drift speed distributions is wide, the majority of drift speeds are well within those derived by Karan et al. (2020) and sources referenced therein: 80–190ms^{-1} (Mendillo & Baumgardner, 1982), 20–100ms^{-1} (Mendillo et al., 1997), -30–150ms^{-1} (Taylor et al., 1997), 40–190ms^{-1} (Sinha & Raizada, 2000), 60–160ms^{-1} (Pimenta et al., 2001), 20–170ms^{-1} (Martinis et al., 2003), 10–125ms^{-1} (Chapagain et al., 2012), 90–190ms^{-1} (Hickey et al., 2018), and -10–125ms^{-1} (Gurav et al., 2019) using ASIs. Marcio et al. (2017) reported average PB drifts between 96–150ms^{-1} with a max of 185ms^{-1} under the southern EIA while England and Immel (2012) used IMAGE-FUV data over the northern EIA to derive drift speeds of 40–160ms^{-1}; well within the bulk of data in figures 10 and 11. Westward drifts mentioned in Taylor et al. (1997) are few in number, but persist for upwards of 90 minutes; well within GOLD's ability to detect.

5.5 Plasma Bubble Widths and Separations

Widths in the range of 100 to 400 km are detected and displayed at the top of figure 12 for both Magnetic region and geographic region. This shows the method is likely limited by GOLD's resolution. Recall GOLD pixel size is ∼95 km at nadir, but can skew upwards of ∼112 km closer to the limb. Ground based observations see scale sizes on the order of 50 to hundreds of kilometers (e.g. (Makela, 2006) and references therein). The separation of PBs should be considered along with these measures of width as GOLD only sees larger bubbles. GOLD may also see 2 PBs that are close together as one.

PB separations are shown in figures 11 and 12. Similar to section 5.4, further subdividing the data by magnetic region, geographic region, or season shows little change in shape, means, and medians, with the exception of June solstice over SA similar to drift speeds. Huang et al. (2012) show irregular longitudinal differences between PBs with data from C/NOFS which appears in figures 11 and 12 by the wide breadth of separation values possible: ∼200 − ∼1200 km for ∼ 90%−∼ 92% of the total separations. Quasiperiodic behavior of PBs observed by Huang et al. (2013) could point to gravity wave seeding with typical separations of 500 − 1000 km which is consistent with GOLD's observations. This may explain why the peaks of the distributions, means, and medians consistently lie within the same range, but would require additional gravity wave data to determine and is not available from GOLD. PBs were detected and analyzed with coincident GOLD, GNSS TEC, SWARM, ionosonde, and cloud temperature data from October 24, 2018 by Aa et al. (2020) which had interbubble distances of 500 − 800 km over the SA and AT regions. This shows the existence of a wide range of PB separations regardless of season or region with a propensity for separations of 500 − 1000 km.

6 Conclusions

An automated method to process GOLD data and detect PBs has been developed in section 3 and implemented in section 4. Simple and robust interpolation methods are used to develop a regular grid (3.2 and 3.3) that are converted to QD coordinates for anal-
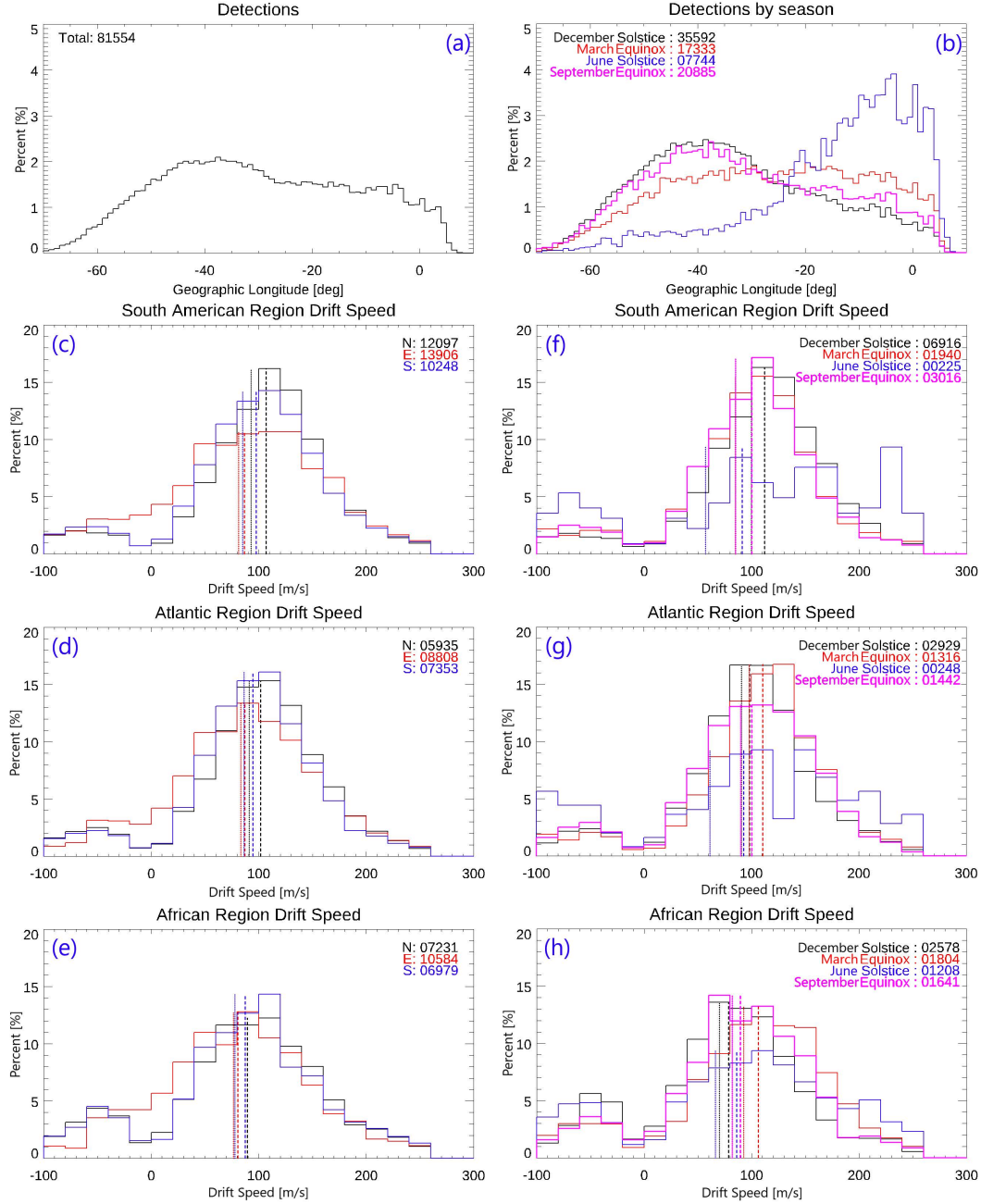
Figure 10. Histograms of PB detections (a – b) and drift speeds by geographic region (c – h). Drift speeds are reported in meters per second. Plot (a) shows detections from the entire database whereas (b) shows detections by season. Plots (c – e) and (f – h) show the geographic regions split by magnetic region and season, respectively. Totals and legends are labeled in the top right of each plot with percent of totals along the y-axis. Magnetic regions are 'N' for QD northern, 'E' for QD equatorial, and 'S' for QD southern region.
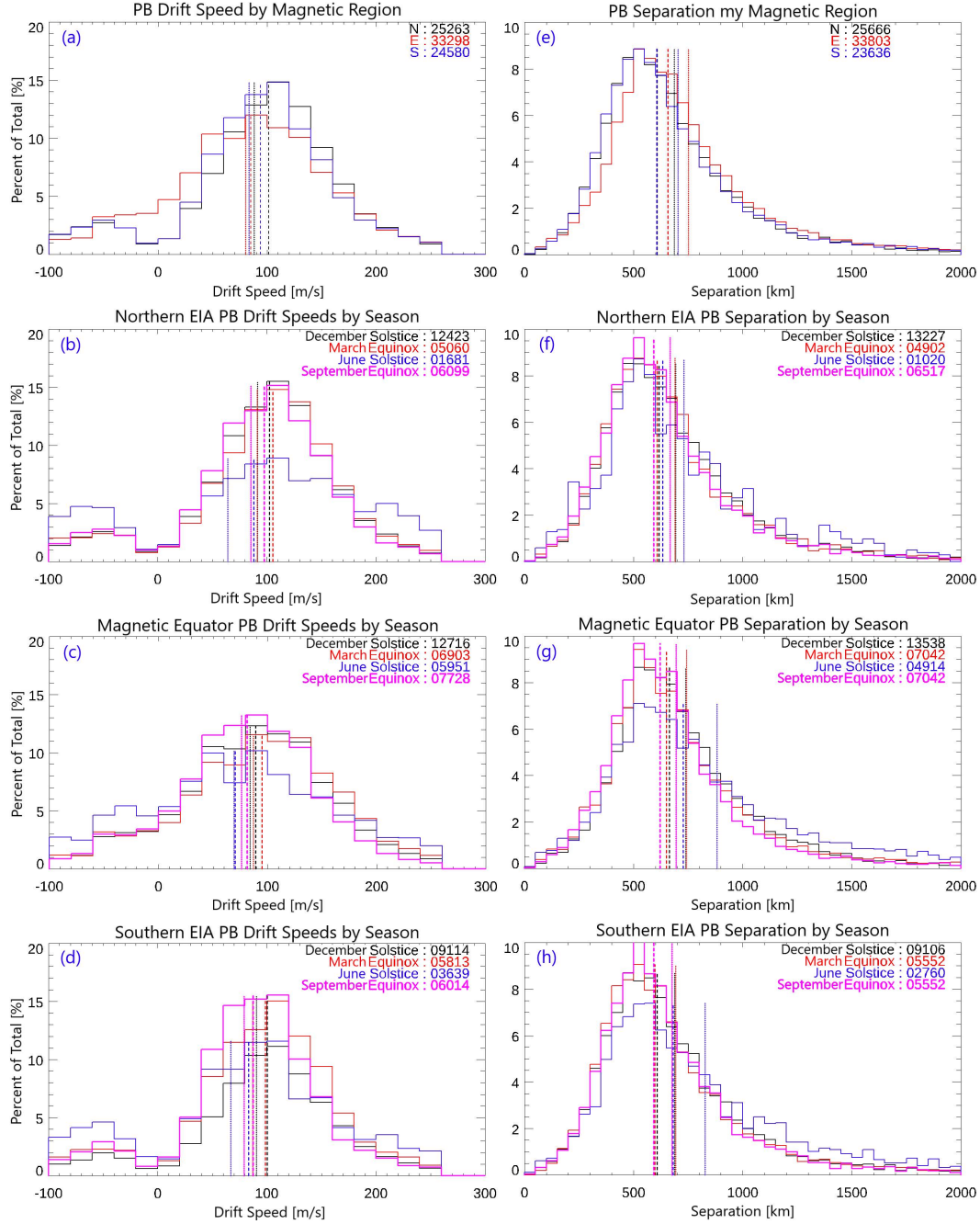
Figure 11. Histograms of PB drift speeds (a – d) and separations (e – h). Drift speeds are reported in meters per second and separations in kilometers. The full database split by magnetic region are shown in (a) and (e): N for QD northern, E for QD equatorial, and S for QD southern region. The following three rows are the northern, equatorial, and southern magnetic regions split by season. Totals and legends are labeled in the top right of each plot with percent of totals along the y-axis.
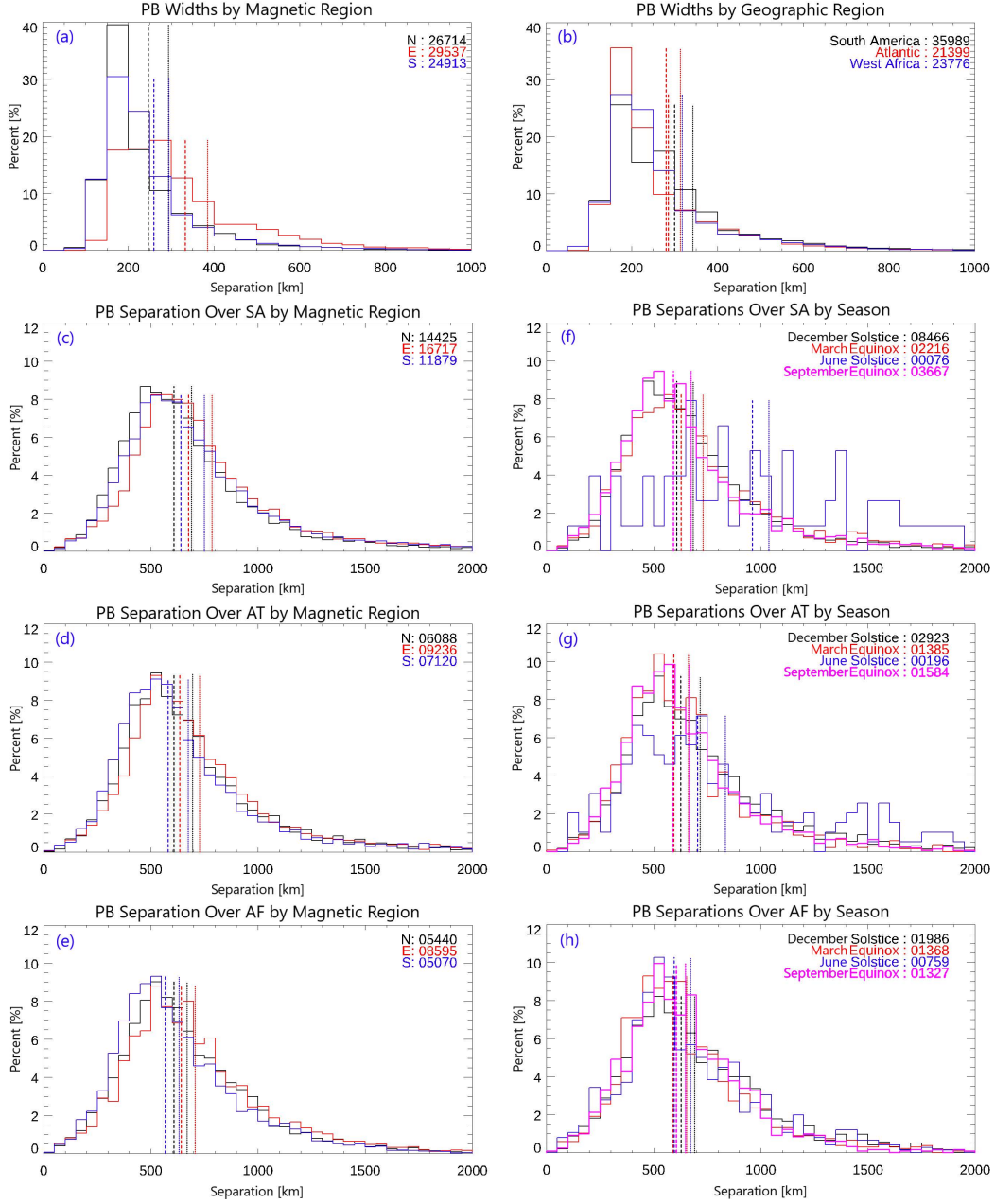
Figure 12. Histograms of PB widths (a – b) and separations (c – h). Widths and separations are reported in kilometers. Plots (a) and (c – e) display widths and separations over geographic regions, respectively, and subdivided by magnetic region: 'N' for northern EIA, 'E' for magnetic equator, 'S' for southern EIA. Plot (b) shows widths by geographic region. Plots (f – h) subdivide separations over geographic regions by season.

ysis (3.4) and combined to form complete north and south images (3.5). Solar and polar influences are removed by implementing a minimum SZA of 107 degrees and QD range of -22 to 22 degrees QDlatitude, respectively (3.6). PB locations are highlighted via difference images generated by detrending of data with RBAVG (3.7). EIA crest tracking ensures equatorial PBs are detected (3.8). An algorithm picks and filters out peaks in difference image summations along QDlatitudes corresponding with PB locations (3.9). These PB locations are used to calculate a measure of width (3.10) and a final database is created (3.11). At the time of writing, this represents the largest such database of PBs from airglow observations currently available.

The database is used to select PBs from distinct images (4.1) to calculate PB drift speeds (4.2), counts (4.3), and separations (4.5). Double counts are removed and uncertainties in geographic coordinates are computed to ensure unique PBs from the database are analyzed with reasonable error bounds (4.4 and 4.6). The results from section 5 are summarized as follows:

- Clear seasonal variation in occurrence of PBs exist with fewer overall occurrences during the June solstice months and the highest during December solstice.
- Slight increases in occurrences can be seen from year to year beyond seasonal variations and are likely due to increased solar activity over the 4 years studied.
- PB occurrences and counts exhibit quasiperiodic behavior in time, regardless of magnetic region.
- Spikes in unique PBs per day occur during both equinoxes and surpass December solstice values.
- Overall occurrences by longitude are level with a slight eastward skew; however, there is a strong seasonal dependence when split by season. PB occurrence skew eastward during December solstice, skew westward during June solstice, and transition during equinoxes.
- PB drift speeds have a wide range of values, but tend toward $\sim$100 ms^{-1}. Further, distributions of drift speeds show little variation by season, geographic region, and magnetic region.
- PB separations have a wide range of values, but tend toward $\sim$500 km. Further, distributions of separations show little variation by season, geographic region, and magnetic region.

Taken together, season have a strong influence on total detections and unique counts of PBs within GOLD's purview; however, PB drift speeds and separations remain largely unaffected by season. This shows the overall behavior of PBs are independent of season, geographic region, or magnetic region.

7 Open Research

Consistent with AGU's FAIR data policy, the PB database generated for this study is available for review at https://figshare.com/s/f2b4649bf5b517f9fdd0. Following acceptance of this manuscript, a formal DOI will be assigned to this dataset, and will appear in the published work.

The GOLD Level 1C NI1 data used to develop the database for this study are available at the GOLD Science Data Center (https://gold.cs.ucf.edu/data/search/) and SPDF (https://spdf.gsfc.nasa.gov/data_orbits.html).

References

Aa, E., Zou, S., Eastes, R., Karan, D. K., Zhang, S.-R., Erickson, P. J., & Coster, A. J. (2020). Coordinated ground-based and space-based observations of equatorial plasma bubbles. *Journal of Geophysical Research: Space Physics*, *125*(1), e2019JA027569. Retrieved from `https://agupubs.onlinelibrary.wiley.com/doi/abs/10.1029/2019JA027569` (e2019JA027569 10.1029/2019JA027569) doi: https://doi.org/10.1029/2019JA027569

Anderson, D. N., & Mendillo, M. (1983). Ionospheric conditions affecting the evolution of equatorial plasma depletions. *Geophysical Research Letters*, *10*(7), 541-544. Retrieved from `https://agupubs.onlinelibrary.wiley.com/doi/abs/10.1029/GL010i007p00541` doi: https://doi.org/10.1029/GL010i007p00541

Aveiro, H. C., Hysell, D. L., Park, J., & Lühr, H. (2011). Equatorial spread f-related currents: Three-dimensional simulations and observations. *Geophysical Research Letters*, *38*(21). Retrieved from `https://agupubs.onlinelibrary.wiley.com/doi/abs/10.1029/2011GL049586` doi: https://doi.org/10.1029/2011GL049586

Chapagain, N. P., Taylor, M. J., Makela, J. J., & Duly, T. M. (2012). Equatorial plasma bubble zonal velocity using 630.0 nm airglow observations and plasma drift modeling over ascension island. *Journal of Geophysical Research: Space Physics*, *117*(A6). Retrieved from `https://agupubs-onlinelibrary-wiley-com.ezproxy.lib.vt.edu/doi/abs/10.1029/2012JA017750` doi: https://doi-org.ezproxy.lib.vt.edu/10.1029/2012JA017750

Comberiate, J., & Paxton, L. J. (2010). Global ultraviolet imager equatorial plasma bubble imaging and climatology, 2002–2007. *Journal of Geophysical Research: Space Physics*, *115*(A4). Retrieved from `https://agupubs.onlinelibrary.wiley.com/doi/abs/10.1029/2009JA014707` doi: https://doi.org/10.1029/2009JA014707

Eastes, R. W., McClintock, W. E., Burns, A. G., Anderson, D. N., Anderson, L., Codrescu, M., ... Oberheide, J. (2017). The global-scale observations of the limb and disk (gold) mission. *Space Science Reviews*, *212*(1), 383–408. Retrieved from `https://doi.org/10.1007/s11214-017-0392-2` doi: 10.1007/s11214-017-0392-2

Eastes, R. W., McClintock, W. E., Burns, A. G., Anderson, D. N., Andersson, L., Aryal, S., ... Woods, T. N. (2020). Initial observations by the gold mission. *Journal of Geophysical Research: Space Physics*, *125*(7), e2020JA027823. Retrieved from `https://agupubs.onlinelibrary.wiley.com/doi/abs/10.1029/2020JA027823` (e2020JA027823 2020JA027823) doi: https://doi.org/10.1029/2020JA027823

Eastes, R. W., Solomon, S. C., Daniell, R. E., Anderson, D. N., Burns, A. G., England, S. L., ... McClintock, W. E. (2019). Global-scale observations of the equatorial ionization anomaly. *Geophysical Research Letters*, *46*(16), 9318-9326. Retrieved from `https://agupubs.onlinelibrary.wiley.com/doi/abs/10.1029/2019GL084199` doi: https://doi.org/10.1029/2019GL084199

England, S. L., & Immel, T. J. (2012). An empirical model of the drift velocity of equatorial plasma depletions. *Journal of Geophysical Research: Space Physics*, *117*(A12). Retrieved from `https://agupubs.onlinelibrary.wiley.com/doi/abs/10.1029/2012JA018091` doi: https://doi.org/10.1029/2012JA018091

Fejer, B. G., de Paula, E. R., González, S. A., & Woodman, R. F. (1991). Average vertical and zonal f region plasma drifts over jicamarca. *Journal of Geophysical Research: Space Physics*, *96*(A8), 13901-13906. Retrieved from `https://agupubs.onlinelibrary.wiley.com/doi/abs/10.1029/91JA01171` doi: https://doi.org/10.1029/91JA01171

Gentile, L. C., Burke, W. J., & Rich, F. J. (2006). A global climatology for equatorial plasma bubbles in the topside ionosphere. *Annales Geophysicae*, *24*(1),

163–172. Retrieved from `https://angeo.copernicus.org/articles/24/163/2006/` doi: 10.5194/angeo-24-163-2006

Gurav, O. B., Narayanan, V. L., K., S. A., Ghodpage, R. N., Gaikwad, H. P., & Patil, P. T. (2019). Airglow imaging observations of some evolutionary aspects of equatorial plasma bubbles from indian sector. *Advances in Space Research, 64*(2), 385-399. Retrieved from `https://www.sciencedirect.com/science/article/pii/S0273117719302510` doi: https://doi.org/10.1016/j.asr.2019.04.008

Hickey, D. A., Martinis, C. R., Mendillo, M., Baumgardner, J., Wroten, J., & Milla, M. (2018). Simultaneous 6300 Å airglow and radar observations of ionospheric irregularities and dynamics at the geomagnetic equator. *Annales Geophysicae, 36*(2), 473-487. doi: https://doi.org/10.5194/angeo-36-473-2018

Huang, C.-S., de La Beaujardiere, O., Roddy, P. A., Hunton, D. E., Ballenthin, J. O., & Hairston, M. R. (2012). Generation and characteristics of equatorial plasma bubbles detected by the c/nofs satellite near the sunset terminator. *Journal of Geophysical Research: Space Physics, 117*(A11). Retrieved from `https://agupubs.onlinelibrary.wiley.com/doi/abs/10.1029/2012JA018163` doi: https://doi.org/10.1029/2012JA018163

Huang, C.-S., de La Beaujardière, O., Roddy, P. A., Hunton, D. E., Ballenthin, J. O., Hairston, M. R., & Pfaff, R. F. (2013). Large-scale quasiperiodic plasma bubbles: C/nofs observations and causal mechanism. *Journal of Geophysical Research: Space Physics, 118*(6), 3602-3612. Retrieved from `https://agupubs.onlinelibrary.wiley.com/doi/abs/10.1002/jgra.50338` doi: https://doi.org/10.1002/jgra.50338

Huang, C.-S., & Roddy, P. A. (2016). Effects of solar and geomagnetic activities on the zonal drift of equatorial plasma bubbles. *Journal of Geophysical Research: Space Physics, 121*(1), 628-637. Retrieved from `https://agupubs.onlinelibrary.wiley.com/doi/abs/10.1002/2015JA021900` doi: https://doi.org/10.1002/2015JA021900

Huba, J. D., Joyce, G., & Krall, J. (2008). Three-dimensional equatorial spread f modeling. *Geophysical Research Letters, 35*(10). Retrieved from `https://agupubs.onlinelibrary.wiley.com/doi/abs/10.1029/2008GL033509` doi: https://doi.org/10.1029/2008GL033509

Hysell, D. L. (2000). An overview and synthesis of plasma irregularities in equatorial spread f. *Journal of Atmospheric and Solar-Terrestrial Physics, 62*(12), 1037-1056. Retrieved from `https://www.sciencedirect.com/science/article/pii/S136468260000095X` doi: https://doi.org/10.1016/S1364-6826(00)00095-X

Immel, T. J., Mende, S. B., Frey, H. U., Peticolas, L. M., & Sagawa, E. (2003). Determination of low latitude plasma drift speeds from fuv images. *Geophysical Research Letters, 30*(18). Retrieved from `https://agupubs.onlinelibrary.wiley.com/doi/abs/10.1029/2003GL017573` doi: https://doi.org/10.1029/2003GL017573

Karan, D. K., Daniell, R. E., England, S. L., Martinis, C. R., Eastes, R. W., Burns, A. G., & McClintock, W. E. (2020). First zonal drift velocity measurement of equatorial plasma bubbles (epbs) from a geostationary orbit using gold data. *Journal of Geophysical Research: Space Physics, 125*(9), e2020JA028173. Retrieved from `https://agupubs.onlinelibrary.wiley.com/doi/abs/10.1029/2020JA028173` (e2020JA028173 2020JA028173) doi: https://doi.org/10.1029/2020JA028173

Keskinen, M. J., Ossakow, S. L., & Fejer, B. G. (2003). Three-dimensional non-linear evolution of equatorial ionospheric spread-f bubbles. *Geophysical Research Letters, 30*(16). Retrieved from `https://agupubs.onlinelibrary.wiley.com/doi/abs/10.1029/2003GL017418` doi: https://doi.org/10.1029/2003GL017418

Keskinen, M. J., & Vadas, S. L. (2009). Three-dimensional nonlinear evolution of equatorial ionospheric bubbles with gravity wave seeding and tidal wind effects. *Geophysical Research Letters*, *36*(12). Retrieved from `https://agupubs.onlinelibrary.wiley.com/doi/abs/10.1029/2009GL037892` doi: https://doi.org/10.1029/2009GL037892

Laundal, K. M., & Richmond, A. D. (2017). Magnetic coordinate systems. *Space Science Reviews*, *206*(1), 27—59. Retrieved from `https://doi.org/10.1007/s11214-016-0275-y` doi: 10.1007/s11214-016-0275-y

Ledvina, B. M., & Makela, J. J. (2005). First observations of sbas/waas scintillations: Using collocated scintillation measurements and all-sky images to study equatorial plasma bubbles. *Geophysical Research Letters*, *32*(14). Retrieved from `https://agupubs.onlinelibrary.wiley.com/doi/abs/10.1029/2004GL021954` doi: https://doi.org/10.1029/2004GL021954

Liu, G., England, S. L., Frey, H. U., Immel, T. J., Lin, C. S., Pacheco, E. E., ... Doornbos, E. (2013). Comparison of drift velocities of nighttime equatorial plasma depletions with ambient plasma drifts and thermospheric neutral winds. *Journal of Geophysical Research: Space Physics*, *118*(11), 7360-7368. Retrieved from `https://agupubs.onlinelibrary.wiley.com/doi/abs/10.1002/2013JA019329` doi: https://doi.org/10.1002/2013JA019329

Magdaleno, S., Herraiz, M., Altadill, D., & de la Morena, B. (2017). Climatology characterization of equatorial plasma bubbles using gps data. *J. Space Weather Space Clim.*, *7*, A3. Retrieved from `https://doi.org/10.1051/swsc/2016039` doi: 10.1051/swsc/2016039

Makela, J. J. (2006). A review of imaging low-latitude ionospheric irregularity processes. *Journal of Atmospheric and Solar-Terrestrial Physics*, *68*(13), 1441-1458. Retrieved from `https://www.sciencedirect.com/science/article/pii/S136468260600109X` doi: https://doi.org/10.1016/j.jastp.2005.04.014

Makela, J. J., Kelley, M. C., & de la Beaujardiére, O. (2006). Convective ionospheric storms: A major space weather problem. *Space Weather*, *4*(2). Retrieved from `https://agupubs.onlinelibrary.wiley.com/doi/abs/10.1029/2005SW000144` doi: https://doi.org/10.1029/2005SW000144

Marcio, T. A. H. M., Duarte-Silva, M., Moraes, A. O., de Paula, E. R., Luiz F C de, R., Alfonsi, L., & Affonso, B. J. (2017). Climatology and modeling of ionospheric scintillations and irregularity zonal drifts at the equatorial anomaly crest region. *Annales Geophysicae*, *35*(6), 1201-1218. Retrieved from `http://login.ezproxy.lib.vt.edu/login?url=https://www.proquest.com/scholarly-journals/climatology-modeling-ionospheric-scintillations/docview/2414611859/se-2`

Martinis, C., Daniell, R., Eastes, R., Norrell, J., Smith, J., Klenzing, J., ... Burns, A. (2021). Longitudinal variation of postsunset plasma depletions from the global-scale observations of the limb and disk (gold) mission. *Journal of Geophysical Research: Space Physics*, *126*(2), e2020JA028510. Retrieved from `https://agupubs.onlinelibrary.wiley.com/doi/abs/10.1029/2020JA028510` doi: https://doi.org/10.1029/2020JA028510

Martinis, C., Eccles, J. V., Baumgardner, J., Manzano, J., & Mendillo, M. (2003). Latitude dependence of zonal plasma drifts obtained from dual-site airglow observations. *Journal of Geophysical Research: Space Physics*, *108*(A3). Retrieved from `https://agupubs-onlinelibrary-wiley-com.ezproxy.lib.vt.edu/doi/abs/10.1029/2002JA009462` doi: https://doi-org.ezproxy.lib.vt.edu/10.1029/2002JA009462

McClintock, W. E., Eastes, R. W., Hoskins, A. C., Siegmund, O. H. W., McPhate, J. B., Krywonos, A., ... Burns, A. G. (2020). Global-scale observations of the limb and disk mission implementation: 1. instrument design and early flight performance. *Journal of Geophysical Research: Space Physics*, *125*(5), e2020JA027797. Retrieved from `https://agupubs.onlinelibrary.wiley`

.com/doi/abs/10.1029/2020JA027797   (e2020JA027797 2020JA027797) doi: https://doi.org/10.1029/2020JA027797

Meier, R. R.   (1991).   Ultraviolet spectroscopy and remote sensing of the upper atmosphere. *Space Science Reviews*, *58*(1).   Retrieved from https://doi.org/10.1007/BF01206000   doi: 10.1007/BF01206000

Mende, S. B., Heetderks, H., Frey, H. U., Stock, J. M., Lampton, M., Geller, S. P., . . . Lauche, H.   (2000).   Far ultraviolet imaging from the image spacecraft. 3. spectral imaging of lyman-α and oi 135.6 nm. *Space Science Reviews*, *91*(1), 287–318. Retrieved from https://doi.org/10.1023/A:1005292301251   doi: 10.1023/A:1005292301251

Mendillo, M., & Baumgardner, J.   (1982).   Airglow characteristics of equatorial plasma depletions. *Journal of Geophysical Research: Space Physics*, *87*(A9), 7641-7652.   Retrieved from https://agupubs.onlinelibrary.wiley.com/doi/abs/10.1029/JA087iA09p07641   doi: https://doi.org/10.1029/JA087iA09p07641

Mendillo, M., Baumgardner, J., Colerico, M., & Nottingham, D.   (1997).   Imaging science contributions to equatorial aeronomy: Initial results from the miseta program. *Journal of Atmospheric and Solar-Terrestrial Physics*, *59*(13), 1587-1599.   Retrieved from https://www.sciencedirect.com/science/article/pii/S1364682696001587   doi: https://doi.org/10.1016/S1364-6826(96)00158-7

Mendillo, M., & Tyler, A. (1983). Geometry of depleted plasma regions in the equatorial ionosphere. *Journal of Geophysical Research: Space Physics*, *88*(A7), 5778-5782.   Retrieved from https://agupubs.onlinelibrary.wiley.com/doi/abs/10.1029/JA088iA07p05778   doi: https://doi.org/10.1029/JA088iA07p05778

Ott, E. (1978). Theory of rayleigh-taylor bubbles in the equatorial ionosphere. *Journal of Geophysical Research: Space Physics*, *83*(A5), 2066-2070.   Retrieved from https://agupubs.onlinelibrary.wiley.com/doi/abs/10.1029/JA083iA05p02066   doi: https://doi.org/10.1029/JA083iA05p02066

Park, J., Mende, S. B., Eastes, R. W., & Frey, H. U.   (2022).   Climatology of equatorial plasma bubbles in ionospheric connection explorer/far-ultraviolet (icon/fuv) limb images. *Journal of Astronomy and Space Sciences*, *39*, 87-98.   Retrieved from http://janss.kr/journal/article.php?code=84158

Park, S. H., England, S. L., Immel, T. J., Frey, H. U., & Mende, S. B.   (2007).   A method for determining the drift velocity of plasma depletions in the equatorial ionosphere using far-ultraviolet spacecraft observations. *Journal of Geophysical Research: Space Physics*, *112*(A11).   Retrieved from https://agupubs.onlinelibrary.wiley.com/doi/abs/10.1029/2007JA012327   doi: https://doi.org/10.1029/2007JA012327

Pimenta, A. A., Fagundes, P. R., Bittencourt, J. A., Sahai, Y., Gobbi, D., Medeiros, A. F., & Taylor, M. J.   (2001).   Ionospheric plasma bubble zonal drift: a methodology using oi 630 nm all-sky imaging systems. *Advances in Space Research*, *27*(6), 1219-1224.   Retrieved from https://www.sciencedirect.com/science/article/pii/S0273117701002010   doi: https://doi.org/10.1016/S0273-1177(01)00201-0

Pradipta, R., Valladares, C. E., & Doherty, P. H.   (2015).   An effective tec data detrending method for the study of equatorial plasma bubbles and traveling ionospheric disturbances. *Journal of Geophysical Research: Space Physics*, *120*(12), 11,048-11,055.   Retrieved from https://agupubs.onlinelibrary.wiley.com/doi/abs/10.1002/2015JA021723   doi: https://doi.org/10.1002/2015JA021723

Sekar, R., Suhasini, R., & Raghavarao, R.   (1995).   Evolution of plasma bubbles in the equatorial f region with different seeding conditions. *Geophysical Research Letters*, *22*(8), 885-888.   Retrieved from https://

agupubs.onlinelibrary.wiley.com/doi/abs/10.1029/95GL00813 doi: https://doi.org/10.1029/95GL00813

Sinha, H. S. S., & Raizada, S. (2000). Some new features of ionospheric plasma depletions over the indian zone using all sky optical imaging. *Earth, Planets and Space*, *52*(8), 549–559. Retrieved from https://doi.org/10.1186/BF03351662 doi: 10.1186/BF03351662

Taylor, M. J., Eccles, J. V., LaBelle, J., & Sobral, J. H. A. (1997). High resolution oi (630 nm) image measurements of f-region depletion drifts during the guará campaign. *Geophysical Research Letters*, *24*(13), 1699-1702. Retrieved from https://agupubs-onlinelibrary-wiley-com.ezproxy.lib.vt.edu/doi/abs/10.1029/97GL01207 doi: https://doi-org.ezproxy.lib.vt.edu/10.1029/97GL01207

Vadas, S. L., & Keskinen, M. J. (2010). Correction to "three-dimensional nonlinear evolution of equatorial ionospheric bubbles with gravity wave seeding and tidal wind effects". *Geophysical Research Letters*, *37*(3). Retrieved from https://agupubs.onlinelibrary.wiley.com/doi/abs/10.1029/2009GL041216 doi: https://doi.org/10.1029/2009GL041216

Wan, X., Xiong, C., Rodriguez-Zuluaga, J., Kervalishvili, G. N., Stolle, C., & Wang, H. (2018). Climatology of the occurrence rate and amplitudes of local time distinguished equatorial plasma depletions observed by swarm satellite. *Journal of Geophysical Research: Space Physics*, *123*(4), 3014-3026. Retrieved from https://agupubs.onlinelibrary.wiley.com/doi/abs/10.1002/2017JA025072 doi: https://doi.org/10.1002/2017JA025072

Weber, E. J., Buchau, J., Eather, R. H., & Mende, S. B. (1978). North-south aligned equatorial airglow depletions. *Journal of Geophysical Research: Space Physics*, *83*(A2), 712-716. Retrieved from https://agupubs.onlinelibrary.wiley.com/doi/abs/10.1029/JA083iA02p00712 doi: https://doi.org/10.1029/JA083iA02p00712

Yokoyama, T., Shinagawa, H., & Jin, H. (2014). Nonlinear growth, bifurcation, and pinching of equatorial plasma bubble simulated by three-dimensional high-resolution bubble model. *Journal of Geophysical Research: Space Physics*, *119*(12), 10,474-10,482. Retrieved from https://agupubs.onlinelibrary.wiley.com/doi/abs/10.1002/2014JA020708 doi: https://doi.org/10.1002/2014JA020708

Zargham, S., & Seyler, C. E. (1989). Collisional and inertial dynamics of the ionospheric interchange instability. *Journal of Geophysical Research: Space Physics*, *94*(A7), 9009-9027. Retrieved from https://agupubs.onlinelibrary.wiley.com/doi/abs/10.1029/JA094iA07p09009 doi: https://doi.org/10.1029/JA094iA07p09009

Figure 1.

Original Data and Interpolants

Original Data and Interpolants (Zoomed In)

Nearest Neighbor Regions

Figure 2.

NN Data Pair and QD Conversion

(a)

(b)

QD Latitude [QDdeg]

QD Longitude [QDdeg]

Intensity [R]

10.00

8.75

7.50

6.25

5.00

3.75

2.50

1.25

0.00

QD and SZA Cutoffs

(c)

(d)

QD Latitude [QDdeg]

QD: [-22,22] [QDdeg]   SZA: [107, 180] [deg]

QD Longitude [QDdeg]

Figure 3.

Rolling Barrel Average Local Level Details

Figure 4.

Smooth Example

(a)

f(x)
Smooth[f(x)] + C
Smooth[f(x)] + C - f(x)

RBAVG Example

(b)

f(x)
RBAVG[f(x)]
RBAVG[f(x)] - f(x)

Radiance Line Plot Along 10 [QDdeg] Latitude

(c)
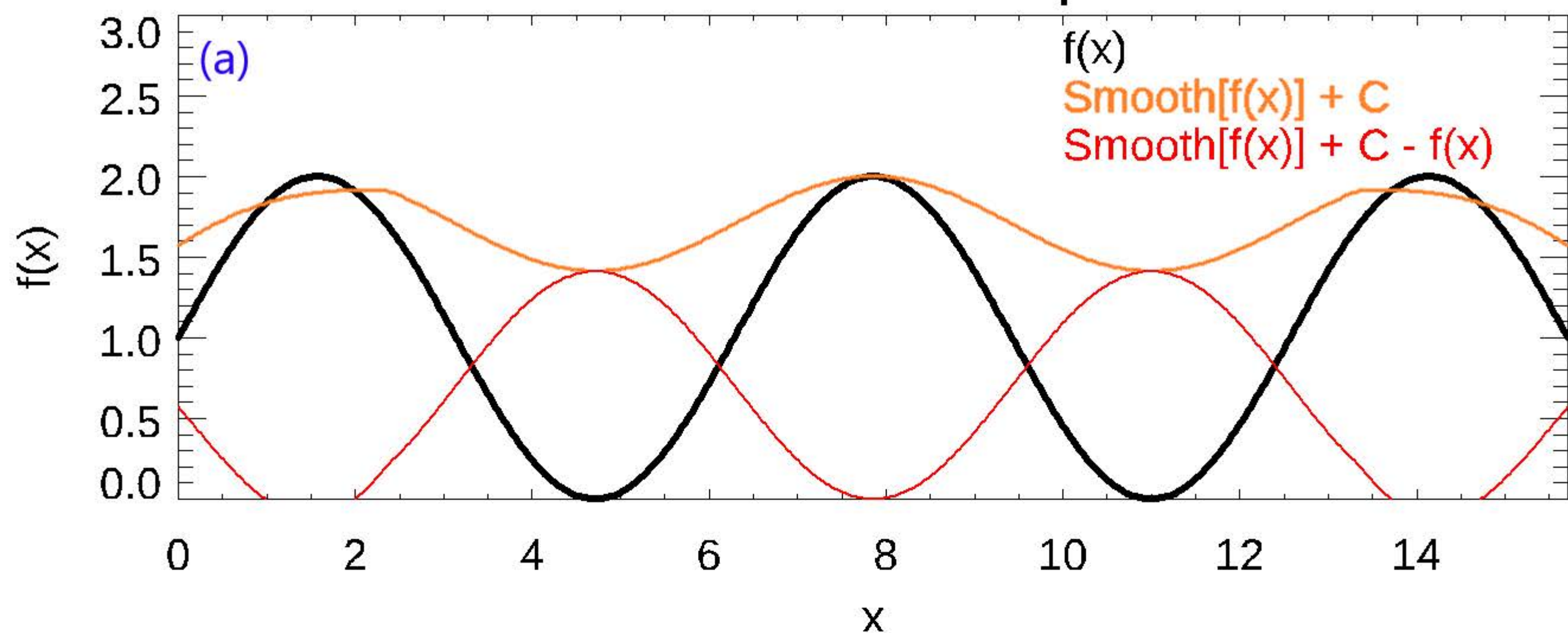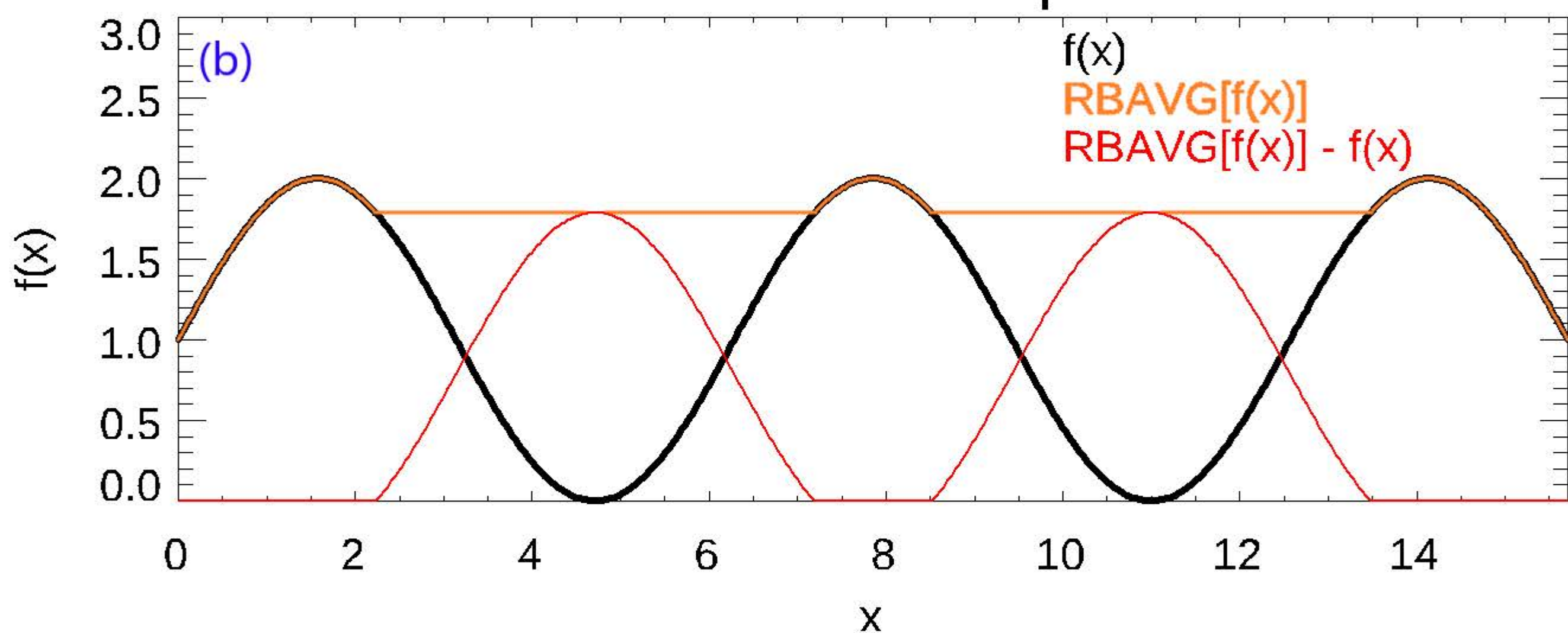
Radiance
RBAVG
Difference
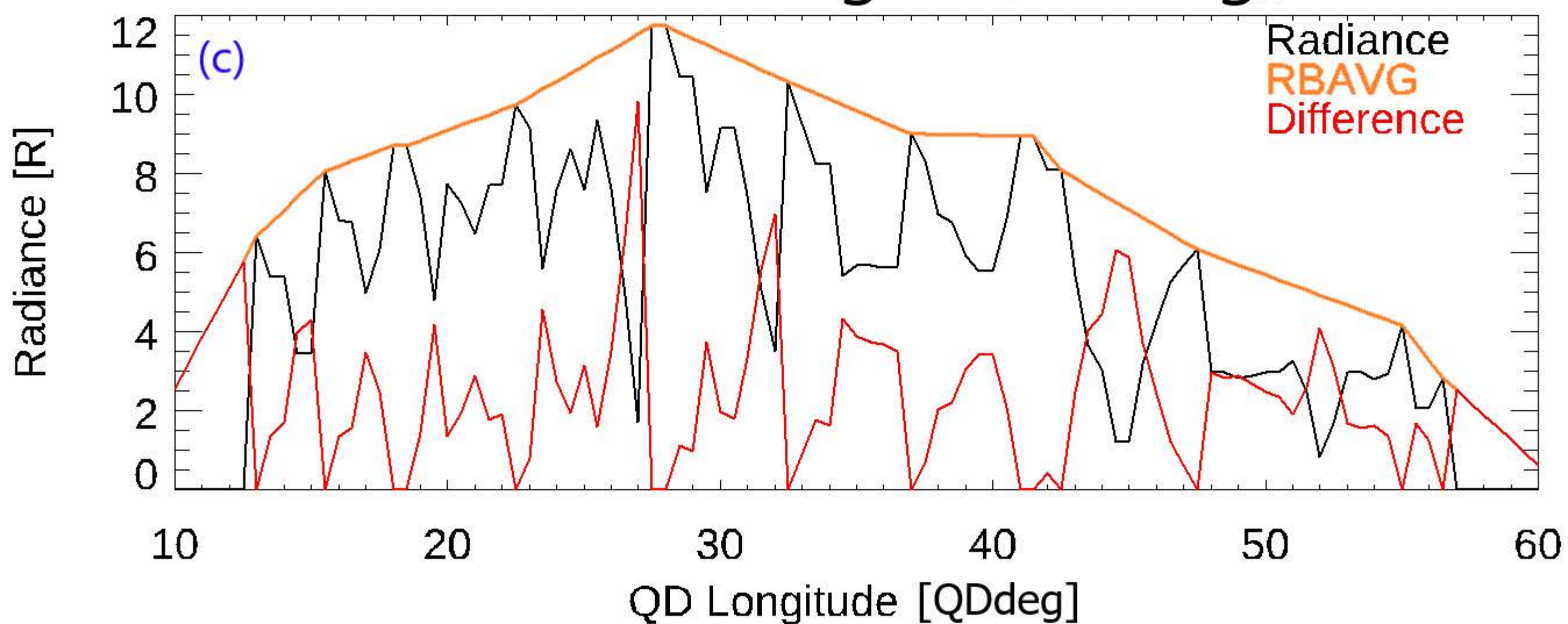
Figure 5.

QD RBAVG and Difference Image
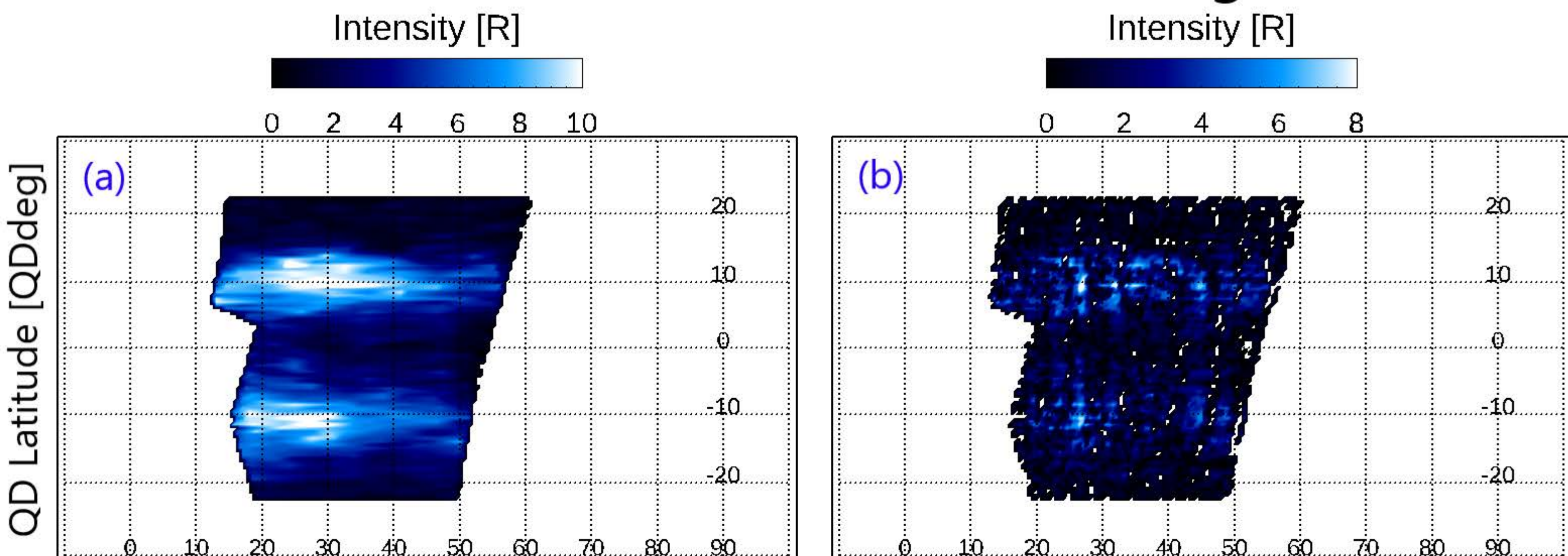
Crest Detection and Line Plot
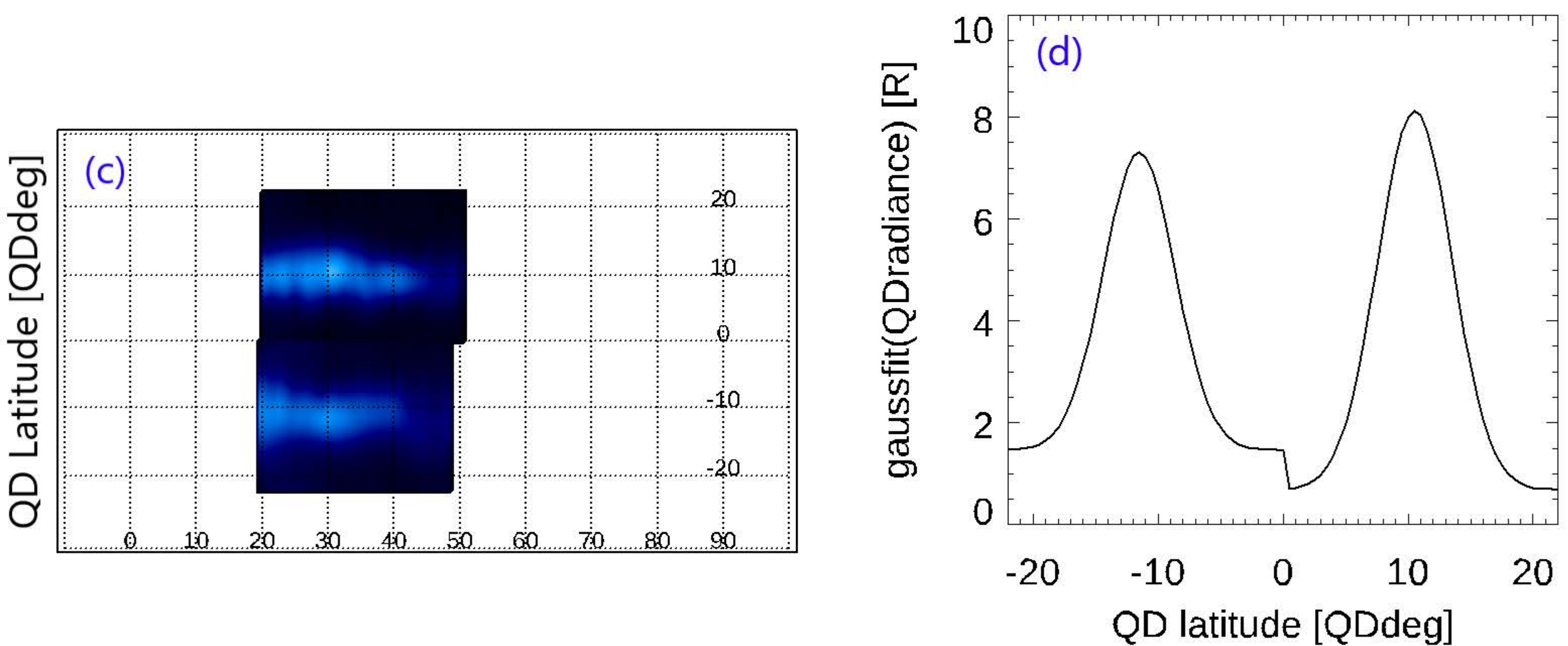
Crest Detection Overlays
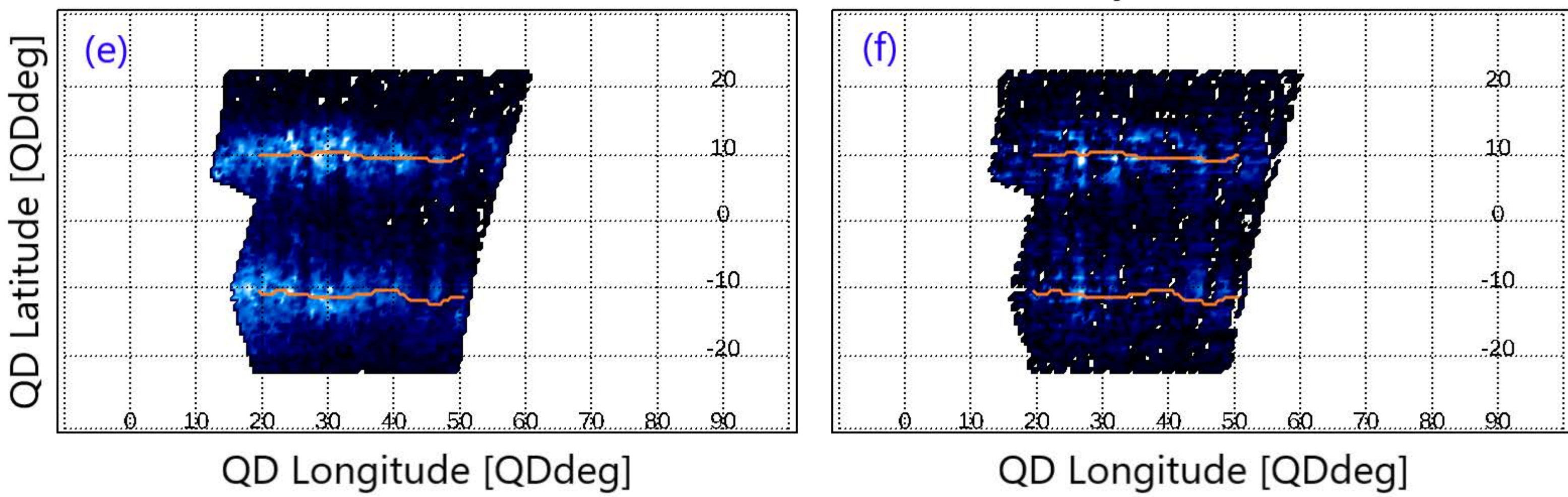
Figure 6.

QD Difference Summation Regions

(a)

QD Latitude [QDdeg]

QD Longitude [QDdeg]

Intensity [R]

Southern Sums: Raw and Filtered

9 detections
7 detections

Peak: * - Raw Sum
Peak: * - Filtered Sum

(b)

Radiance [R]

QD Longitude [QDdeg]

Southern Uncertainty Analysis

4 detections
3 detections

Peak Kept: * - Filtered Sum
Peak Removed: * - Filtered Sum

(c)

Radiance [R]
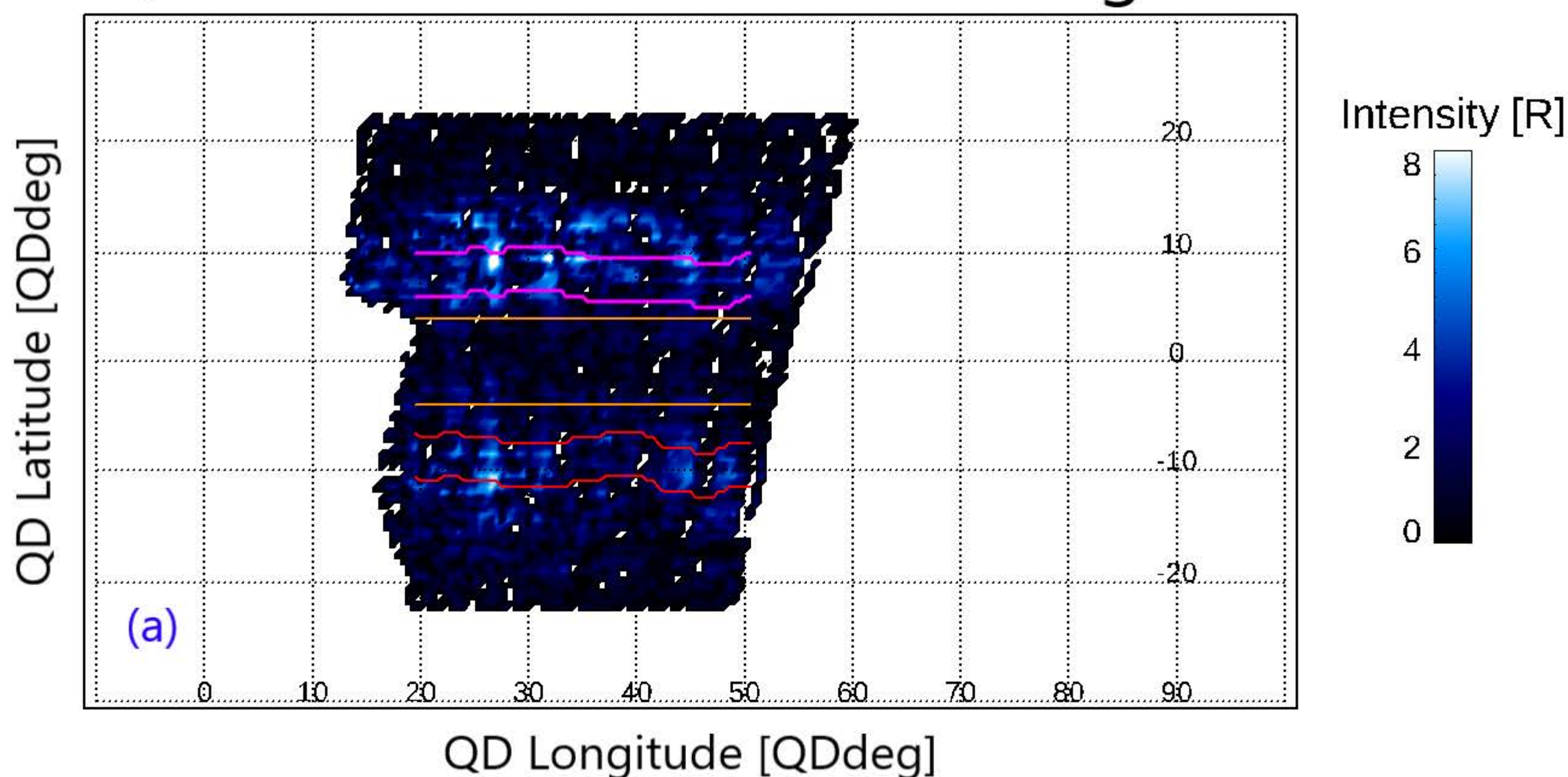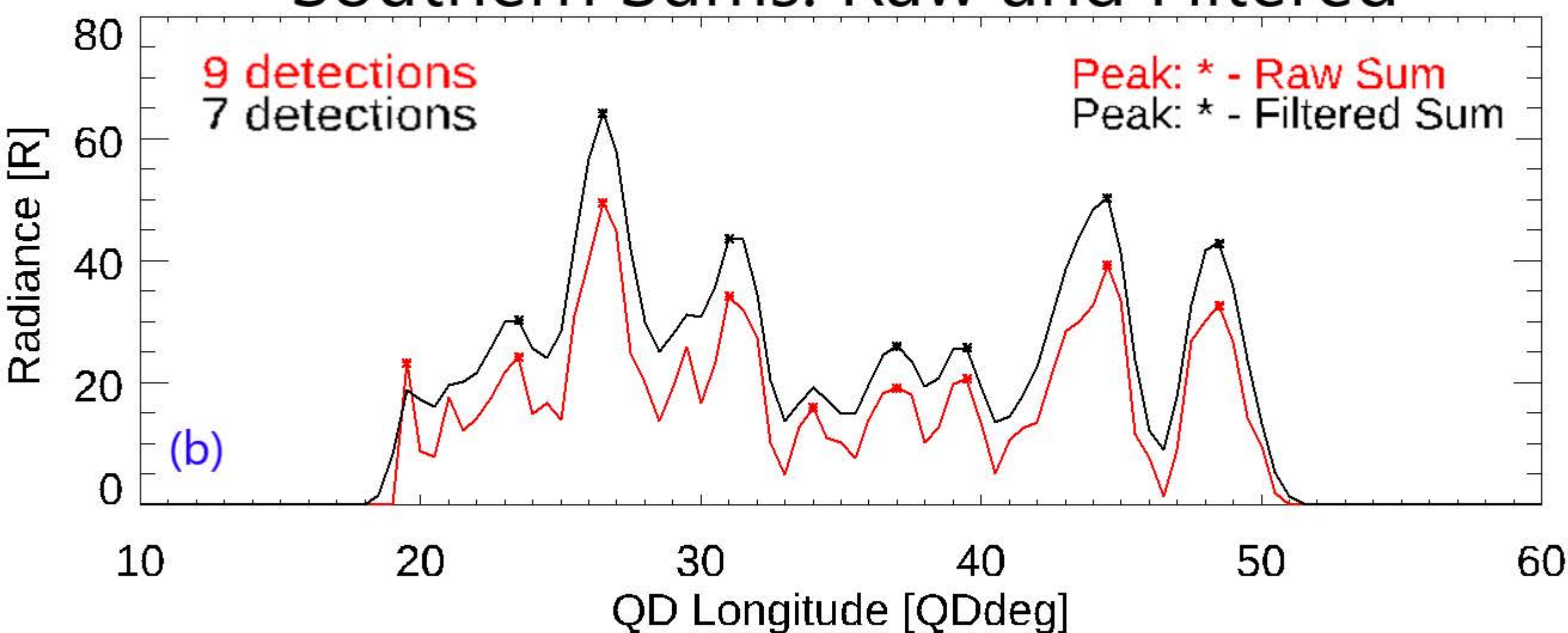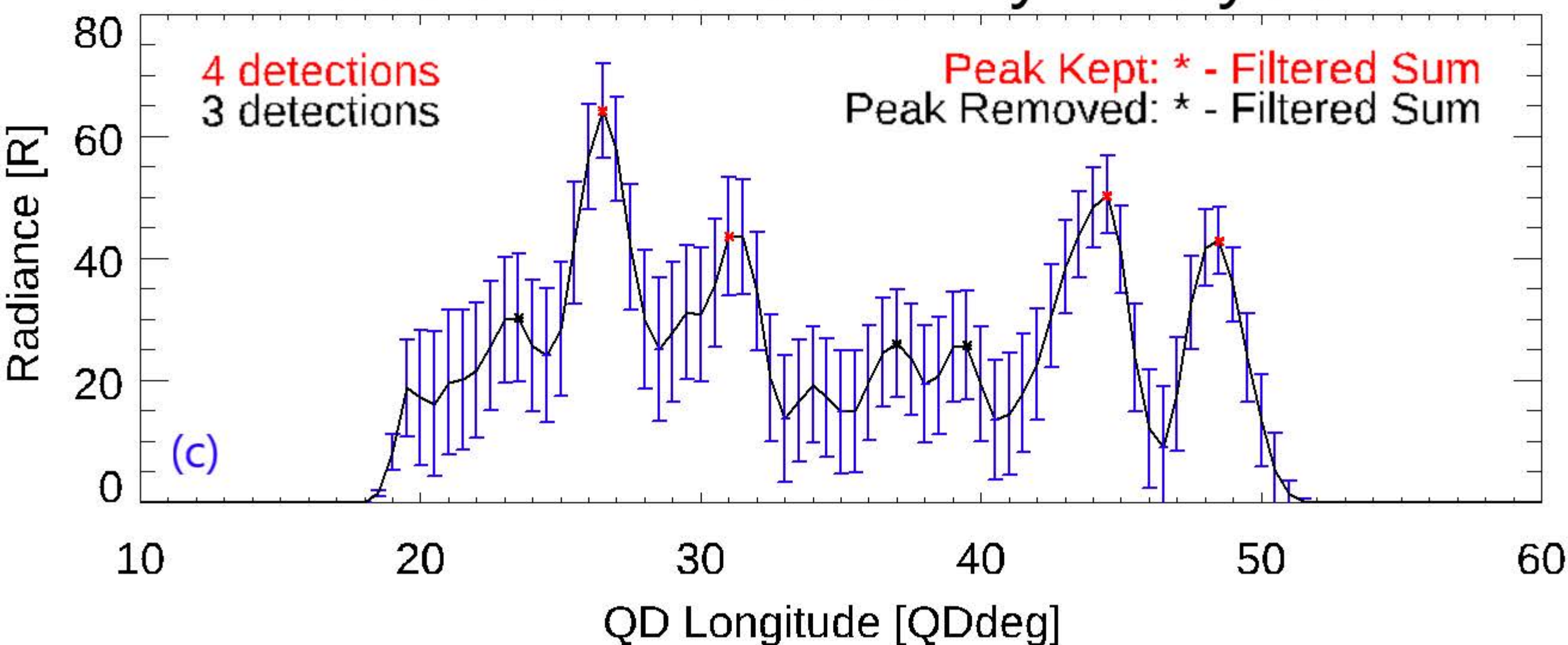
QD Longitude [QDdeg]

Figure 7.

Gaussian Fits Over Peaks

(a)

Peak: * - Filtered Sum
Peak: * - Gaussfit

Radiance [R]

QD Longitude [QDdeg]

Final Image Used for Detection

(b)

(c)

QD Latitude [QDdeg]

* : Detected Bubbles
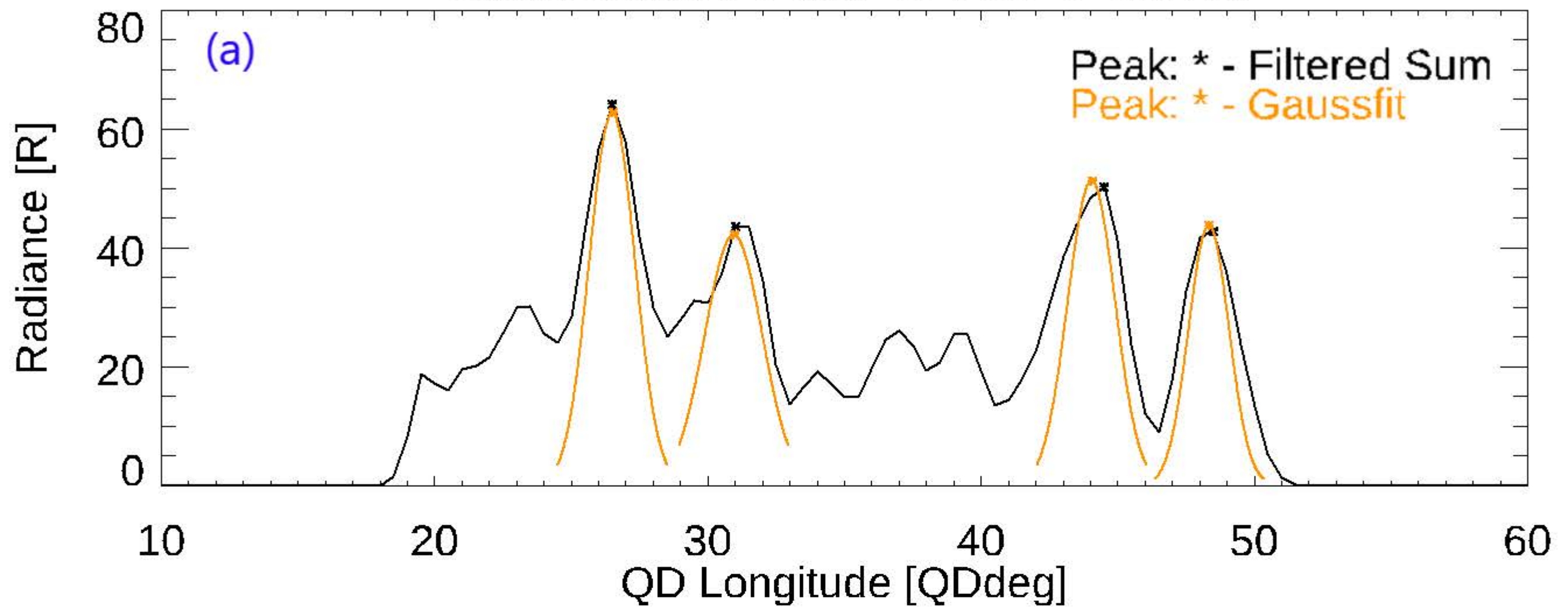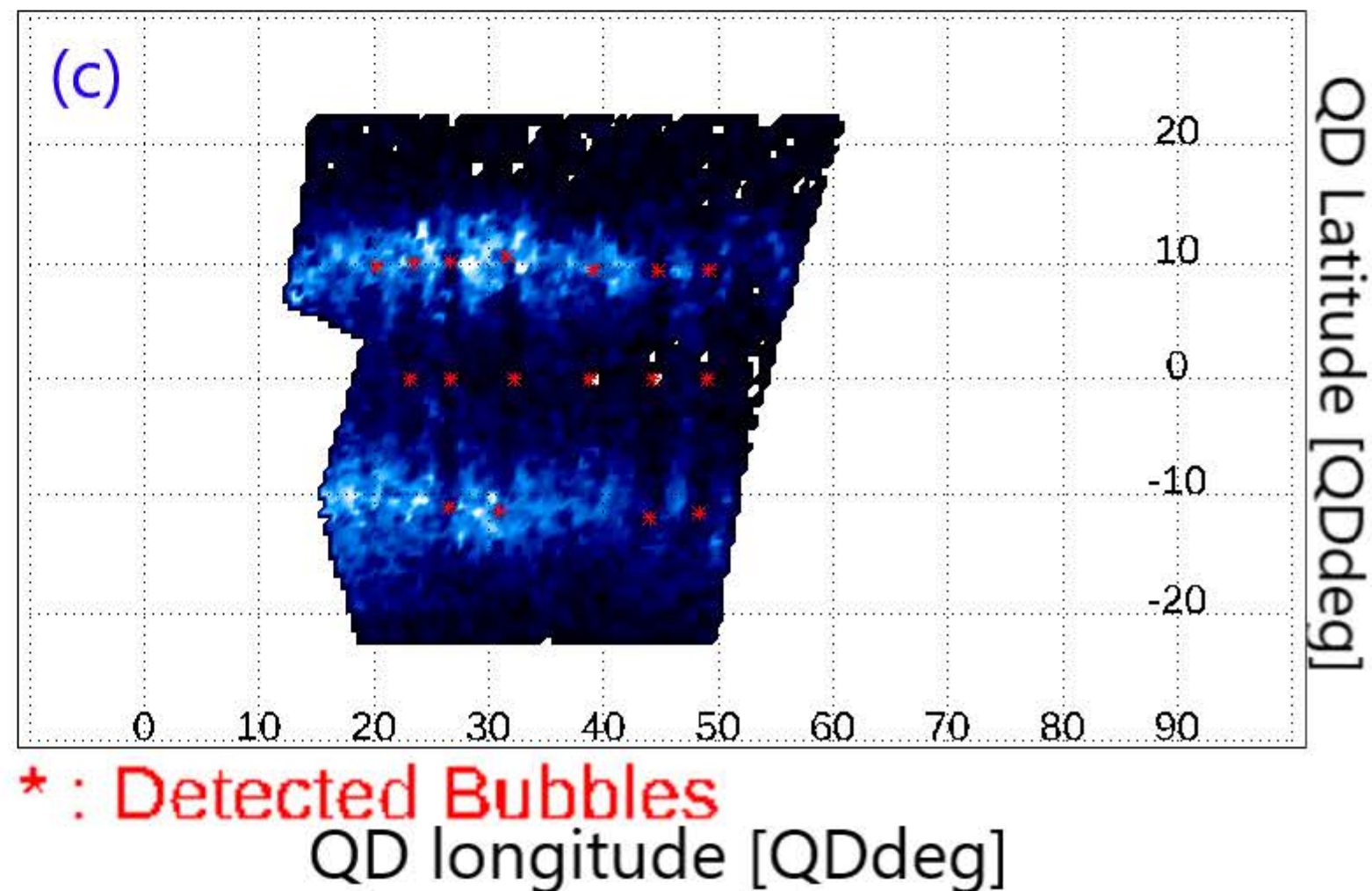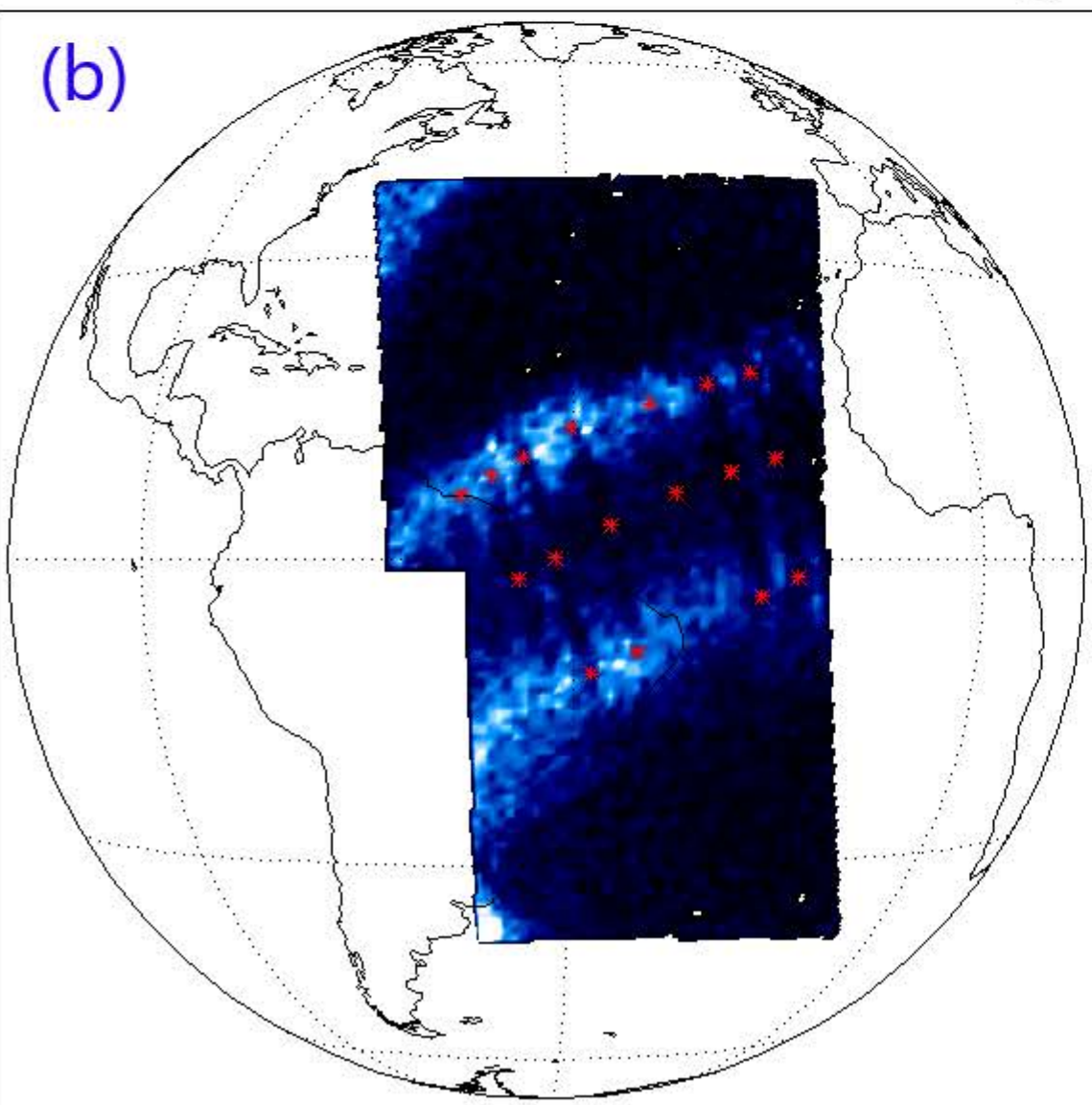
QD longitude [QDdeg]

Figure 8.

Image Pairs for November 28, 2018

2325-N , 2325-S

(a)

2325-S , 2340-N

(b)

2340-N , 2340-S

(c)

2340-S , 2355-N

(d)

QD Latitude [QDdeg]

QD Longitude [QDdeg]

QD Longitude [QDdeg]

Intensity [R]

0   2   4   6   8

PB Drift Speeds from 2325 to 2340 of November 28, 2018

(e)

Northern EIA
Magnetic Equator
Southern EIA

Drift Speed [m/s]

QD Longitude [QDdeg]

PB Separations from November 28, 2018 at 2340

(f)

Northern EIA
Magnetic Equator
Southern EIA

PB separation [km]

QD Longitude [QDdeg]

Figure 9.

PB Detections: December Solstice (a)

PB Detections: March Equinox (b)

PB Detections: June Solstice (c)

PB Detections: September Equinox (d)

Detections

Total Detections per Night: QD-North (e)

Bubbles Detected per Night: QD-North (h)

Total Detections per Night: QD-Equator (f)

Bubbles Detected per Night: QD-Equator (i)

Total Detections per Night: QD-South (g)

Bubbles Detected per Night: QD-South (j)

Figure 10.

Detections

Total: 81554

(a)

Percent [%] vs Geographic Longitude [deg]

Detections by season

December Solstice : 35592
March Equinox : 17333
June Solstice : 07744
SeptemberEquinox : 20885

(b)

Percent [%] vs Geographic Longitude [deg]

South American Region Drift Speed

(c)

N: 12097
E: 13906
S: 10248

Percent [%] vs Drift Speed [m/s]

South American Region Drift Speed

(f)

December Solstice : 06916
March Equinox : 01940
June Solstice : 00225
SeptemberEquinox : 03016

Percent [%] vs Drift Speed [m/s]

Atlantic Region Drift Speed

(d)

N: 05935
E: 08808
S: 07353

Percent [%] vs Drift Speed [m/s]

Atlantic Region Drift Speed

(g)

December Solstice : 02929
March Equinox : 01316
June Solstice : 00248
SeptemberEquinox : 01442

Percent [%] vs Drift Speed [m/s]

African Region Drift Speed

(e)

N: 07231
E: 10584
S: 06979

Percent [%] vs Drift Speed [m/s]

African Region Drift Speed

(h)

December Solstice : 02578
March Equinox : 01804
June Solstice : 01208
SeptemberEquinox : 01641

Percent [%] vs Drift Speed [m/s]

Figure 11.

Figure 12.